

Event Horizon Telescope observations of the jet launching and collimation in Centaurus A

Michael Janssen^{1,2*}, Heino Falcke², Matthias Kadler³, Eduardo Ros¹, Maciek Wielgus^{4,5}, Kazunori Akiyama^{6,7,4}, Mislav Baloković^{8,9}, Lindy Blackburn^{4,5}, Katherine L. Bouman^{4,5,10}, Andrew Chael^{11,12}, Chi-kwan Chan^{13,14}, Koushik Chatterjee¹⁵, Jordy Davelaar^{16,17,2}, Philip G. Edwards¹⁸, Christian M. Fromm^{4,5,19}, José L. Gómez²⁰, Ciriaco Goddi^{2,21}, Sara Issaoun², Michael D. Johnson^{4,5}, Junhan Kim^{13,10}, Jun Yi Koay²², Thomas P. Krichbaum¹, Jun Liu¹, Elisabetta Liuzzo²³, Sera Markoff^{15,24}, Alex Markowitz²⁵, Daniel P. Marrone¹³, Yosuke Mizuno^{26,19}, Cornelia Müller^{1,2}, Chunchong Ni^{27,28}, Dominic W. Pesce^{4,5}, Venkatesh Ramakrishnan²⁹, Freek Roelofs^{5,2}, Kazi L. J. Rygl²³, Ilse van Bemmel³⁰, Antxon Alberdi²⁰, Walter Alef¹, Juan Carlos Algaba³¹, Richard Anantua^{4,5,17}, Keiichi Asada²², Rebecca Azulay^{32,33,1}, Anne-Kathrin Baczko¹, David Ball¹³, John Barrett⁶, Bradford A. Benson^{34,35}, Dan Bintley³⁶, Raymond Blundell⁵, Wilfred Boland³⁷, Geoffrey C. Bower³⁸, Hope Boyce^{39,49}, Michael Bremer⁴¹, Christiaan D. Brinkerink², Roger Brissenden^{4,5}, Silke Britzen¹, Avery E. Broderick^{42,27,28}, Dominique Brogiere⁴¹, Thomas Bronzwaer², Do-Young Byun^{43,44}, John E. Carlstrom^{45,35,46,47}, Shami Chatterjee⁴⁸, Ming-Tang Chen³⁸, Yongjun Chen^{49,50}, Paul M. Chesler⁴, Ilje Cho^{43,44}, Pierre Christian⁵¹, John E. Conway⁵², James M. Cordes⁵³, Thomas M. Crawford^{35,45}, Geoffrey B. Crew⁶, Alejandro Cruz-Osorio¹⁹, Yuzhu Cui^{54,55}, Mariafelicia De Laurentis^{56,19,57}, Roger Deane^{58,59,60}, Jessica Dempsey³⁶, Gregory Desvignes⁶¹, Jason Dexter⁶², Sheperd S. Doeleman^{4,5}, Ralph P. Eatough^{63,1}, Joseph Farah^{5,4,64}, Vincent L. Fish⁶, Ed Fomalont⁶⁵, H. Alyson Ford⁶⁶, Raquel Fraga-Encinas², Per Friberg³⁶, Antonio Fuentes²⁰, Peter Galison^{4,67,68}, Charles F. Gammie^{69,70}, Roberto García⁴¹, Zachary Gelles^{5,4}, Olivier Gentaz⁴¹, Boris Georgiev^{27,28}, Roman Gold^{71,42}, Arturo I. Gómez-Ruiz^{72,73}, Minfeng Gu^{49,74}, Mark Gurwell⁵, Kazuhiro Hada^{54,55}, Daryl Haggard^{39,40}, Michael H. Hecht⁶, Ronald Hesper⁷⁵, Elizabeth Himwich^{76,4}, Luis C. Ho^{77,78}, Paul Ho²², Mareki Honma^{54,55,79}, Chih-Wei L. Huang²², Lei Huang^{49,74}, David H. Hughes⁷², Shiro Ikeda^{7,80,81,82}, Makoto Inoue²², David J. James^{4,5}, Buell T. Jannuzi¹³, Britton Jeter^{27,28}, Wu Jiang⁴⁹, Alejandra Jimenez-Rosales², Svetlana Jorstad^{83,84}, Taehyun Jung^{43,44}, Mansour Karami^{42,27}, Ramesh Karuppusamy¹, Tomohisa Kawashima⁸⁵, Garrett K. Keating⁵, Mark Kettenis³⁰, Dong-Jin Kim¹, Jae-Young Kim^{43,1}, Jongsoo Kim⁴³, Motoki Kino^{7,86}, Yutaro Kofuji^{54,79}, Shoko Koyama²², Michael Kramer¹, Carsten Kramer⁴¹, Cheng-Yu Kuo^{87,22}, Tod R. Lauer⁸⁸, Sang-Sung Lee⁴³, Aviad Levis¹⁰, Yan-Rong Li⁸⁹, Zhiyuan Li^{90,91}, Michael Lindqvist⁵², Rocco Lico^{20,1}, Greg Lindahl⁵, Kuo Liu¹, Wen-Ping Lo^{22,92}, Andrei P. Lobanov¹, Laurent Loinard^{93,94}, Colin Lonsdale⁶, Ru-Sen Lu^{49,50,1}, Nicholas R. MacDonald¹, Jirong Mao^{95,96,97}, Nicola Marchili^{23,1}, Alan P. Marscher⁸³, Iván Martí-Vidal^{32,33}, Satoki Matsushita²², Lynn D. Matthews⁶, Lia Medeiros^{98,13}, Karl M. Menten¹, Izumi Mizuno³⁶, James M. Moran^{4,5}, Kotaro Moriyama^{6,54}, Monika Moscibrodzka², Gibwa Musoke^{15,2}, Alejandro Mus Mejías^{32,33}, Hiroshi Nagai^{7,55}, Neil M. Nagar²⁹, Masanori Nakamura^{99,22}, Ramesh Narayan^{4,5}, Gopal Narayanan¹⁰⁰, Iniyan Natarajan^{60,58,101}, Antonios Nathanail^{19,102}, Joey Neilsen¹⁰³, Roberto Neri⁴¹, Aristeidis Noutsos¹, Michael A. Nowak¹⁰⁴, Hiroki Okino^{54,79}, Héctor Olivares², Gisela N. Ortiz-León¹, Tomoaki Oyama⁵⁴, Feryal Özel¹³, Daniel C. M. Palumbo^{4,5}, Jongho Park^{22,105}, Nimesh Patel⁵, Ue-Li Pen^{42,106,107,108}, Vincent Piétu⁴¹, Richard Plambeck¹⁰⁹, Aleksandar PopStefanija¹⁰⁰, Oliver Porth^{15,19}, Felix M. Pötzl¹, Ben Prather⁶⁹, Jorge A. Preciado-López⁴², Dimitrios Psaltis¹³, Hung-Yi Pu^{110,22,42}, Ramprasad Rao³⁸, Mark G. Rawlings³⁶, Alexander W. Raymond^{4,5}, Luciano Rezzolla^{19,111,112}, Angelo Ricarte^{4,5}, Bart Ripperda^{113,17}, Alan Rogers⁶, Mel Rose¹³, Arash Roshanineshat¹³, Helge

Rottmann¹, Alan L. Roy¹, Chet Ruszczyk⁶, Salvador Sánchez¹¹⁴, David Sánchez-Arguelles^{72,73}, Mahito Sasada^{54,115}, Tuomas Savolainen^{116,117,1}, F. Peter Schloerb¹⁰⁰, Karl-Friedrich Schuster⁴¹, Lijing Shao^{1,78}, Zhiqiang Shen^{49,59}, Des Small³⁰, Bong Won Sohn^{43,44,118}, Jason SooHoo⁶, He Sun¹⁰, Fumie Tazaki⁵⁴, Alexandra J. Tetarenko¹¹⁹, Paul Tiede^{27,28}, Remo P. J. Tilanus^{2,21,120,13}, Michael Titus⁶, Pablo Torne^{1,114}, Tyler Trent¹³, Efthalia Traianou¹, Sascha Trippe¹²¹, Huib Jan van Langevelde^{30,122}, Daniel R. van Rossum², Jan Wagner¹, Derek Ward-Thompson¹²³, John Wardle¹²⁴, Jonathan Weintraub^{4,5}, Norbert Wex¹, Robert Wharton¹, George N. Wong⁶⁹, Qingwen Wu¹²⁵, Doosoo Yoon¹⁵, André Young², Ken Young⁵, Ziri Younsi^{126,19,127}, Feng Yuan^{49,74,128}, Ye-Fei Yuan¹²⁹, J. Anton Zensus¹, Guang-Yao Zhao²⁰, and Shan-Shan Zhao^{49,(**)}

¹Max-Planck-Institut für Radioastronomie, Auf dem Hügel 69, D-53121 Bonn, Germany

²Department of Astrophysics, Institute for Mathematics, Astrophysics and Particle Physics (IMAPP), Radboud University, P.O. Box 9010, 6500 GL Nijmegen, The Netherlands

³Lehrstuhl für Astronomie, Universität Würzburg, Emil-Fischer Str. 31, 97074 Würzburg, Germany

⁴Black Hole Initiative at Harvard University, 20 Garden Street, Cambridge, MA 02138, USA

⁵Center for Astrophysics | Harvard & Smithsonian, 60 Garden Street, Cambridge, MA 02138, USA

⁶Massachusetts Institute of Technology Haystack Observatory, 99 Millstone Road, Westford, MA 01886, USA

⁷National Astronomical Observatory of Japan, 2-21-1 Osawa, Mitaka, Tokyo 181-8588, Japan

⁸Yale Center for Astronomy & Astrophysics, 52 Hillhouse Avenue, New Haven, CT 06511, USA

⁹Department of Physics, Yale University, P.O. Box 2018120, New Haven, CT 06520, USA

¹⁰California Institute of Technology, 1200 East California Boulevard, Pasadena, CA 91125, USA

¹¹Princeton Center for Theoretical Science, Jadwin Hall, Princeton University, Princeton, NJ 08544, USA

¹²NASA Hubble Fellowship Program, Einstein Fellow

¹³Steward Observatory and Department of Astronomy, University of Arizona, 933 N. Cherry Ave., Tucson, AZ 85721, USA

¹⁴Data Science Institute, University of Arizona, 1230 N. Cherry Ave., Tucson, AZ 85721, USA

¹⁵Anton Pannekoek Institute for Astronomy, University of Amsterdam, Science Park 904, 1098 XH, Amsterdam, The Netherlands

¹⁶Department of Astronomy and Columbia Astrophysics Laboratory, Columbia University, 550 W 120th Street, New York, NY 10027, USA

¹⁷Center for Computational Astrophysics, Flatiron Institute, 162 Fifth Avenue, New York, NY 10010, USA

¹⁸Australia Telescope National Facility, CSIRO Astronomy and Space Science, Epping, NSW 1710, Australia

¹⁹Institut für Theoretische Physik, Goethe-Universität Frankfurt, Max-von-Laue-Straße 1, D-60438 Frankfurt am Main, Germany

²⁰Instituto de Astrofísica de Andalucía-CSIC, Glorieta de la Astronomía s/n, E-18008 Granada, Spain

²¹Leiden Observatory—Allegro, Leiden University, P.O. Box 9513, 2300 RA Leiden, The Netherlands

²²Institute of Astronomy and Astrophysics, Academia Sinica, 11F of Astronomy-Mathematics Building, AS/NTU No. 1, Sec. 4, Roosevelt Rd, Taipei 10617, Taiwan, R.O.C.

²³Italian ALMA Regional Centre, INAF-Istituto di Radioastronomia, Via P. Gobetti 101, I-40129 Bologna, Italy

²⁴Gravitation Astroparticle Physics Amsterdam (GRAPPA) Institute, University of Amsterdam, Science Park 904, 1098 XH Amsterdam, The Netherlands

²⁵Nicolaus Copernicus Astronomical Center, Polish Academy of Sciences, Bartycka 18, PL-00-716 Warszawa, Poland

²⁶Tsung-Dao Lee Institute and School of Physics and Astronomy, Shanghai Jiao Tong University, Shanghai, 200240, People's Republic of China

²⁷Department of Physics and Astronomy, University of Waterloo, 200 University Avenue West, Waterloo, ON, N2L 3G1, Canada

²⁸Waterloo Centre for Astrophysics, University of Waterloo, Waterloo, ON, N2L 3G1, Canada

²⁹Astronomy Department, Universidad de Concepción, Casilla 160-C, Concepción, Chile

³⁰Joint Institute for VLBI ERIC (JIVE), Oude Hoogeveensedijk 4, 7991 PD Dwingeloo, The Netherlands

³¹Department of Physics, Faculty of Science, University of Malaya, 50603 Kuala Lumpur, Malaysia

³²Departament d'Astronomia i Astrofísica, Universitat de València, C. Dr. Moliner 50, E-46100 Burjassot, València, Spain

³³Observatori Astronòmic, Universitat de València, C. Catedrático José Beltrán 2, E-46980 Paterna, València, Spain

³⁴Fermi National Accelerator Laboratory, MS209, P.O. Box 500, Batavia, IL, 60510, USA

³⁵Department of Astronomy and Astrophysics, University of Chicago, 5640 South Ellis Avenue, Chicago, IL, 60637, USA

³⁶East Asian Observatory, 660 N. A'ohoku Place, Hilo, HI 96720, USA

³⁷Nederlandse Onderzoekschool voor Astronomie (NOVA), PO Box 9513, 2300 RA Leiden, The Netherlands

³⁸Institute of Astronomy and Astrophysics, Academia Sinica, 645 N. A'ohoku Place, Hilo, HI 96720, USA

³⁹Department of Physics, McGill University, 3600 rue University, Montréal, QC H3A 2T8, Canada

⁴⁰McGill Space Institute, McGill University, 3550 rue University, Montréal, QC H3A 2A7, Canada

⁴¹Institut de Radioastronomie Millimétrique, 300 rue de la Piscine, F-38406 Saint Martin d'Hères, France

- ⁴² *Perimeter Institute for Theoretical Physics, 31 Caroline Street North, Waterloo, ON, N2L 2Y5, Canada*
- ⁴³ *Korea Astronomy and Space Science Institute, Daedeok-daero 776, Yuseong-gu, Daejeon 34055, Republic of Korea*
- ⁴⁴ *University of Science and Technology, Gajeong-ro 217, Yuseong-gu, Daejeon 34113, Republic of Korea*
- ⁴⁵ *Kavli Institute for Cosmological Physics, University of Chicago, 5640 South Ellis Avenue, Chicago, IL, 60637, USA*
- ⁴⁶ *Department of Physics, University of Chicago, 5720 South Ellis Avenue, Chicago, IL 60637, USA*
- ⁴⁷ *Enrico Fermi Institute, University of Chicago, 5640 South Ellis Avenue, Chicago, IL 60637, USA*
- ⁴⁸ *Cornell Center for Astrophysics and Planetary Science, Cornell University, Ithaca, NY 14853, USA*
- ⁴⁹ *Shanghai Astronomical Observatory, Chinese Academy of Sciences, 80 Nandan Road, Shanghai 200030, People's Republic of China*
- ⁵⁰ *Key Laboratory of Radio Astronomy, Chinese Academy of Sciences, Nanjing 210008, People's Republic of China*
- ⁵¹ *Physics Department, Fairfield University, 1073 North Benson Road, Fairfield, CT 06824, USA*
- ⁵² *Department of Space, Earth and Environment, Chalmers University of Technology, Onsala Space Observatory, SE-43992 Onsala, Sweden*
- ⁵³ *Cornell Center for Astrophysics and Planetary Science, Cornell University, Ithaca, NY 14853, USA*
- ⁵⁴ *Mizusawa VLBI Observatory, National Astronomical Observatory of Japan, 2-12 Hoshigaoka, Mizusawa, Oshu, Iwate 023-0861, Japan*
- ⁵⁵ *Department of Astronomical Science, The Graduate University for Advanced Studies (SOKENDAI), 2-21-1 Osawa, Mitaka, Tokyo 181-8588, Japan*
- ⁵⁶ *Dipartimento di Fisica "E. Pancini", Università di Napoli "Federico II", Compl. Univ. di Monte S. Angelo, Edificio G, Via Cinthia, I-80126, Napoli, Italy*
- ⁵⁷ *INFN Sez. di Napoli, Compl. Univ. di Monte S. Angelo, Edificio G, Via Cinthia, I-80126, Napoli, Italy*
- ⁵⁸ *Wits Centre for Astrophysics, University of the Witwatersrand, 1 Jan Smuts Avenue, Braamfontein, Johannesburg 2050, South Africa*
- ⁵⁹ *Department of Physics, University of Pretoria, Hatfield, Pretoria 0028, South Africa*
- ⁶⁰ *Centre for Radio Astronomy Techniques and Technologies, Department of Physics and Electronics, Rhodes University, Makhanda 6140, South Africa*
- ⁶¹ *LESIA, Observatoire de Paris, Université PSL, CNRS, Sorbonne Université, Université de Paris, 5 place Jules Janssen, 92195 Meudon, France*
- ⁶² *JILA and Department of Astrophysical and Planetary Sciences, University of Colorado, Boulder, CO 80309, USA*
- ⁶³ *National Astronomical Observatories, Chinese Academy of Sciences, 20A Datun Road, Chaoyang District, Beijing 100101, PR China*
- ⁶⁴ *University of Massachusetts Boston, 100 William T. Morrissey Boulevard, Boston, MA 02125, USA*
- ⁶⁵ *National Radio Astronomy Observatory, 520 Edgemont Rd, Charlottesville, VA 22903, USA*
- ⁶⁶ *Steward Observatory and Department of Astronomy, University of Arizona, 933 N. Cherry Avenue, Tucson, AZ 85721, USA*
- ⁶⁷ *Department of History of Science, Harvard University, Cambridge, MA 02138, USA*
- ⁶⁸ *Department of Physics, Harvard University, Cambridge, MA 02138, USA*
- ⁶⁹ *Department of Physics, University of Illinois, 1110 West Green Street, Urbana, IL 61801, USA*
- ⁷⁰ *Department of Astronomy, University of Illinois at Urbana-Champaign, 1002 West Green Street, Urbana, IL 61801, USA*
- ⁷¹ *CP3-Origins, University of Southern Denmark, Campusvej 55, DK-5230 Odense M, Denmark*
- ⁷² *Instituto Nacional de Astrofísica, Óptica y Electrónica. Apartado Postal 51 y 216, 72000. Puebla Pue., México*
- ⁷³ *Consejo Nacional de Ciencia y Tecnología, Av. Insurgentes Sur 1582, 03940, Ciudad de México, México*
- ⁷⁴ *Key Laboratory for Research in Galaxies and Cosmology, Chinese Academy of Sciences, Shanghai 200030, People's Republic of China*
- ⁷⁵ *NOVA Sub-mm Instrumentation Group, Kapteyn Astronomical Institute, University of Groningen, Landleven 12, 9747 AD Groningen, The Netherlands*
- ⁷⁶ *Center for the Fundamental Laws of Nature, Harvard University, Cambridge, MA 02138, USA*
- ⁷⁷ *Department of Astronomy, School of Physics, Peking University, Beijing 100871, People's Republic of China*
- ⁷⁸ *Kavli Institute for Astronomy and Astrophysics, Peking University, Beijing 100871, People's Republic of China*
- ⁷⁹ *Department of Astronomy, Graduate School of Science, The University of Tokyo, 7-3-1 Hongo, Bunkyo-ku, Tokyo 113-0033, Japan*
- ⁸⁰ *The Institute of Statistical Mathematics, 10-3 Midori-cho, Tachikawa, Tokyo, 190-8562, Japan*
- ⁸¹ *Department of Statistical Science, The Graduate University for Advanced Studies (SOKENDAI), 10-3 Midori-cho, Tachikawa, Tokyo 190-8562, Japan*
- ⁸² *Kavli Institute for the Physics and Mathematics of the Universe, The University of Tokyo, 5-1-5 Kashiwanoha, Kashiwa, 277-8583, Japan*
- ⁸³ *Institute for Astrophysical Research, Boston University, 725 Commonwealth Ave., Boston, MA 02215, USA*
- ⁸⁴ *Astronomical Institute, St. Petersburg University, Universitetskij pr., 28, Petrodvorets, 198504 St. Petersburg, Russia*
- ⁸⁵ *Institute for Cosmic Ray Research, The University of Tokyo, 5-1-5 Kashiwanoha, Kashiwa, Chiba 277-8582, Japan*
- ⁸⁶ *Kogakuin University of Technology & Engineering, Academic Support Center, 2665-1 Nakano, Hachioji, Tokyo 192-0015, Japan*
- ⁸⁷ *Physics Department, National Sun Yat-Sen University, No. 70, Lien-Hai Rd, Kaosiung City 80424, Taiwan, R.O.C*

- ⁸⁸ *National Optical Astronomy Observatory, 950 N. Cherry Ave., Tucson, AZ 85719, USA*
- ⁸⁹ *Key Laboratory for Particle Astrophysics, Institute of High Energy Physics, Chinese Academy of Sciences, 19B Yuquan Road, Shijingshan District, Beijing, People's Republic of China*
- ⁹⁰ *School of Astronomy and Space Science, Nanjing University, Nanjing 210023, People's Republic of China*
- ⁹¹ *Key Laboratory of Modern Astronomy and Astrophysics, Nanjing University, Nanjing 210023, People's Republic of China*
- ⁹² *Department of Physics, National Taiwan University, No.1, Sect.4, Roosevelt Rd., Taipei 10617, Taiwan, R.O.C*
- ⁹³ *Instituto de Radioastronomía y Astrofísica, Universidad Nacional Autónoma de México, Morelia 58089, México*
- ⁹⁴ *Instituto de Astronomía, Universidad Nacional Autónoma de México, CdMx 04510, México*
- ⁹⁵ *Yunnan Observatories, Chinese Academy of Sciences, 650011 Kunming, Yunnan Province, People's Republic of China*
- ⁹⁶ *Center for Astronomical Mega-Science, Chinese Academy of Sciences, 20A Datun Road, Chaoyang District, Beijing, 100012, People's Republic of China*
- ⁹⁷ *Key Laboratory for the Structure and Evolution of Celestial Objects, Chinese Academy of Sciences, 650011 Kunming, People's Republic of China*
- ⁹⁸ *School of Natural Sciences, Institute for Advanced Study, 1 Einstein Drive, Princeton, NJ 08540, USA*
- ⁹⁹ *National Institute of Technology, Hachinohe College, 16-1 Uwanotai, Tamonoki, Hachinohe City, Aomori 039-1192, Japan*
- ¹⁰⁰ *Department of Astronomy, University of Massachusetts, 01003, Amherst, MA, USA*
- ¹⁰¹ *South African Radio Astronomy Observatory, Observatory 7925, Cape Town, South Africa*
- ¹⁰² *Department of Physics, National and Kapodistrian University of Athens, Panepistimiopolis, GR 15783 Zografos, Greece*
- ¹⁰³ *Villanova University, Mendel Science Center Rm. 263B, 800 E Lancaster Ave, Villanova PA 19085*
- ¹⁰⁴ *Physics Department, Washington University CB 1105, St Louis, MO 63130, USA*
- ¹⁰⁵ *EACOA fellow*
- ¹⁰⁶ *Canadian Institute for Theoretical Astrophysics, University of Toronto, 60 St. George Street, Toronto, ON M5S 3H8, Canada*
- ¹⁰⁷ *Dunlap Institute for Astronomy and Astrophysics, University of Toronto, 50 St. George Street, Toronto, ON M5S 3H4, Canada*
- ¹⁰⁸ *Canadian Institute for Advanced Research, 180 Dundas St West, Toronto, ON M5G 1Z8, Canada*
- ¹⁰⁹ *Radio Astronomy Laboratory, University of California, Berkeley, CA 94720, USA*
- ¹¹⁰ *Department of Physics, National Taiwan Normal University, No. 88, Sec.4, Tingzhou Rd., Taipei 116, Taiwan, R.O.C.*
- ¹¹¹ *Frankfurt Institute for Advanced Studies, Ruth-Moufang-Strasse 1, 60438 Frankfurt, Germany*
- ¹¹² *School of Mathematics, Trinity College, Dublin 2, Ireland*
- ¹¹³ *Department of Astrophysical Sciences, Peyton Hall, Princeton University, Princeton, NJ 08544, USA*
- ¹¹⁴ *Instituto de Radioastronomía Milimétrica, IRAM, Avenida Divina Pastora 7, Local 20, E-18012, Granada, Spain*
- ¹¹⁵ *Hiroshima Astrophysical Science Center, Hiroshima University, 1-3-1 Kagamiyama, Higashi-Hiroshima, Hiroshima 739-8526, Japan*
- ¹¹⁶ *Aalto University Department of Electronics and Nanoengineering, PL 15500, FI-00076 Aalto, Finland*
- ¹¹⁷ *Aalto University Metsähovi Radio Observatory, Metsähovintie 114, FI-02540 Kylmäla, Finland*
- ¹¹⁸ *Department of Astronomy, Yonsei University, Yonsei-ro 50, Seodaemun-gu, 03722 Seoul, Republic of Korea*
- ¹¹⁹ *East Asian Observatory, 660 North A'ohoku Place, Hilo, HI 96720, USA*
- ¹²⁰ *Netherlands Organisation for Scientific Research (NWO), Postbus 93138, 2509 AC Den Haag, The Netherlands*
- ¹²¹ *Department of Physics and Astronomy, Seoul National University, Gwanak-gu, Seoul 08826, Republic of Korea*
- ¹²² *Leiden Observatory, Leiden University, Postbus 2300, 9513 RA Leiden, The Netherlands*
- ¹²³ *Jeremiah Horrocks Institute, University of Central Lancashire, Preston PR1 2HE, UK*
- ¹²⁴ *Physics Department, Brandeis University, 415 South Street, Waltham, MA 02453, USA*
- ¹²⁵ *School of Physics, Huazhong University of Science and Technology, Wuhan, Hubei, 430074, People's Republic of China*
- ¹²⁶ *Mullard Space Science Laboratory, University College London, Holmbury St. Mary, Dorking, Surrey, RH5 6NT, UK*
- ¹²⁷ *UKRI Stephen Hawking Fellow*
- ¹²⁸ *School of Astronomy and Space Sciences, University of Chinese Academy of Sciences, No. 19A Yuquan Road, Beijing 100049, People's Republic of China*
- ¹²⁹ *Astronomy Department, University of Science and Technology of China, Hefei 230026, People's Republic of China*
- * *Corresponding author. Email: mjanssen@mpifr-bonn.mpg.de*
- (**) *The Event Horizon Telescope Collaboration*

Very-long-baseline interferometry (VLBI) observations of active galactic nuclei at millimeter wavelengths have the power to reveal the launching and initial collimation region of extragalactic radio jets, down to $10\text{--}100$ gravitational radii ($r_g \equiv GM/c^2$) scales in nearby sources¹. Centaurus A is the closest radio-loud source to Earth². It bridges the gap in mass and accretion rate between the supermassive black holes (SMBHs) in Messier 87 and our galactic center. A large southern declination of -43° has however prevented VLBI imaging of Centaurus A below $\lambda 1\text{ cm}$ thus far. Here, we show the millimeter VLBI image of the source, which we obtained with the Event Horizon Telescope at 228 GHz. Compared to previous observations³, we image Centaurus A’s jet at a tenfold higher frequency and sixteen times sharper resolution and thereby probe sub-lightday structures. We reveal a highly-collimated, asymmetrically edge-brightened jet as well as the fainter counterjet. We find that Centaurus A’s source structure resembles the jet in Messier 87 on $\sim 500 r_g$ scales remarkably well. Furthermore, we identify the location of Centaurus A’s SMBH with respect to its resolved jet core at $\lambda 1.3\text{ mm}$ and conclude that the source’s event horizon shadow⁴ should be visible at THz frequencies. This location further supports the universal scale invariance of black holes over a wide range of masses^{5,6}.

In this work, we present the first image of Centaurus A (Cen A) obtained by the Event Horizon Telescope (EHT) with a nominal resolution of 25 microarcseconds (μas) at $\lambda 1.3\text{ mm}$. For a black hole mass of $(5.5 \pm 3) \times 10^7 M_\odot$ ⁷, we are probing jet structures down to scales of $\sim 200 r_g \approx 0.6$ light days. It has recently become possible to model these scales with sophisticated general relativistic magnetohydrodynamics (GRMHD) simulations⁸, where jet ejection and their symbiotic relationship with accretion flows are simulated from first principles. We have observed Cen A in a six-hour-long track on April 10, 2017. The EHT, as a novel and heterogeneous high-frequency VLBI array, poses unique calibration challenges. To obtain robust results, independent of assumptions made during the data calibration, we base our scientific analysis on two data sets, which we obtained from two independent calibration pipelines: rPICARD⁹ and EHT-HOPS¹⁰ (Methods 1.1.2).

Figure 1 presents our reconstruction of the jet image structure derived from the EHT data using a regularized maximum-likelihood method, next to the large-scale source morphology and the similarly edge-brightened morphology of the M87 jet on comparable gravitational scales. These images are convolved with Gaussian beams set by their respective nominal instrumental resolutions, as per standard practice in radio-interferometric imaging, to suppress possibly spurious fine-scale structures in the image model. The brightness temperatures \mathcal{T} [K] shown are related to flux densities S in jansky (Jy) through the observing wavelength λ , Boltzmann constant k_B , and angular resolution element Ω as $\mathcal{T} = \lambda^2 (2k_B\Omega)^{-1} S$. The $\lambda 1.3\text{ mm}$ Cen A jet has a narrow, collimated profile and exhibits one-sidedness, pronounced edge-brightening, and a northwest-southeast (NW-SE) brightness asymmetry. The approaching jet extends towards the north-east and the faint counterjet is directed south-westwards. The total compact flux density in our image is $\sim 2\text{ Jy}$. The identification of the jet apex and black hole position (Methods 1.4.1) is shown in the unconvolved image model of Figure 2. We can use interferometer data with a high signal-to-noise ratio to super-resolve image features beyond the nominal resolution of the instrument. We therefore base our analysis on the robust features of the unconvolved image model. We have verified the robustness of the counterjet feature with synthetic data studies (Supplementary Fig. 4). The estimated jet position angle (PA) on the sky of $48^\circ \pm 5^\circ$ agrees with cm-wave VLBI observations³. The cm-band data also constrain the inclination angle of the jet axis with respect to our line of sight to $\theta \sim 12^\circ\text{--}45^\circ$, assuming the jet does not bend along the line of sight.

The Cen A $\lambda 1.3\text{ mm}$ jet exhibits three types of brightness asymmetries (\mathcal{R}): between the jet and counterjet, the sheath and spine, and the NW vs. SE ridgelines (Methods 1.4.2). We take the two bright radiating streams of the approaching- and counter-jet as jet ‘arms’ and denote the maximum intensity region along each arm as ‘ridgeline’. The jet-to-counterjet intensity ratio $\mathcal{R}_{j/cj}$ can naturally be explained for a relativistic outflow with $\theta \neq 90^\circ$, where jet emission will be Doppler boosted and counterjet emission de-boosted. We find $\mathcal{R}_{j/cj} \gtrsim 5$, which is in agreement with cm-wave VLBI observations³ and suggests that the initial acceleration of the jet occurs within the inner collimation region imaged in this study.

There is no jet spine emission in our image. With synthetic data studies, we found that spine emission exceeding $\sim 20\%$ of the sheath radiation intensity would be detectable, i.e., $\mathcal{R}_{sh/sp} > 5$ (Methods 1.3). The intensities of the brightest, central SE and NW jet components in the unconvolved image are $(32 \pm 8) \times 10^9\text{ K}$ and $(20 \pm 4) \times 10^9\text{ K}$, respectively. The brightness ratio between these components follows as $\mathcal{R}_{s/n} = 1.6 \pm 0.5$.

The collimation profile of the jet width W follows a narrow expansion profile with distance to the apex z as $W \propto z^k$ with $k = 0.33 \pm 0.05|_{\text{stat}} \pm 0.06|_{\text{sys}}$ (Figure 3). Resolution and potentially optical depth effects prevent us from pinning down the jet opening angle ψ_{jet} at small z , where the jet converges towards the apex. We denote the boundary between the inner convergence region and the outer jet with a clearly defined collimation and easily

traceable jet ridgelines as z_{col} . For the brighter and straighter SE arm, we have $W(z_{\text{col}} \approx 32 \mu\text{as}) \approx 25 \mu\text{as}$, i.e., the brightest jet component marks the boundary between the convergence and strongly collimated regions here (Figure 2). If we assume the two jet ridgelines to meet at the apex, we find $\psi_{\text{jet}} \gtrsim 40^\circ$ as a conservative estimate. Factoring in the range of possible θ values yields $\psi_{\text{int}} \gtrsim 10^\circ - 30^\circ$ for the intrinsic, deprojected opening angle (Methods 1.4.3).

The M 87¹¹ (NGC 4486, 3C 274, Virgo A), Markarian 501¹², and restarted 3C 84 jets¹³ also show strong edge-brightening and large initial opening angles on comparable scales seen at similar inclination angles of $\sim 18^\circ$. The expansion profile of Cen A lies in between the parabolic profile of M 87 ($k = 0.5$) and the almost cylindrical profile of 3C 84 ($k = 0.2$), which implies a strong confinement of the 3C 84 jet by a shallow pressure gradient from the ambient medium. For the inner Cen A jet, this suggests strong magnetic collimation or the presence of external pressure and density gradients of $P_{\text{ext}} \propto z^{-4k} = z^{-1.3}$ and $\rho_{\text{ext}} \propto z^{1-4k} = z^{-0.3}$ (Methods 1.4.4). Radiatively inefficient accretion flows alone, which are expected to operate in the M 87, 3C 84, and Cen A sub-Eddington low-luminosity AGN (LLAGN) sources, have comparatively steeper pressure and density gradients¹⁴. This may indicate the presence of winds, which are likely to be launched by this type of accretion flow. The noticeable similarity and prominence of edge-brightened jet emission in M 87, 3C 84, and Cen A suggests the dominance of jet sheath emission to be an emerging feature in LLAGN. In GRMHD simulations, the sheath manifests itself as interaction region between an accretion-powered outflow¹⁵ and the fast jet spine, which is potentially powered by the black hole spin¹⁶. The mass-loaded sheath has a higher intrinsic emissivity compared to the evacuated spine. The same type of LLAGN-applicable GRMHD simulations also self-consistently develop a collimating helical magnetic field structure in the jet, which is confirmed observationally in many active galactic nuclei (AGN)¹⁷. The dominating sheath emissivity and helical magnetic field structure provides a natural intrinsic explanation for the prevailing edge-brightening in LLAGN and can also explain the NW-SE brightness asymmetry. This model and alternative geometric explanations for the brightness asymmetries are discussed in the Methods 1.4.2 section.

The basic radiative properties of these jets can be analytically understood with a simple model¹⁸, where particle and magnetic energy density equipartition is assumed, while the particle density decays with z^{-2} . Under these conditions, an optically thick and self-absorbed compact feature is expected (the core), whose position z_{core} along the jet is frequency dependent with $z_{\text{core}} \propto \nu^{-1}$ ^{19,20}. This radio core corresponds to the photosphere, where the optical depth $\tau(\nu)$ to photons at the observing frequency ν is unity. The jet is optically thick upstream and optically thin downstream. The photosphere moves closer to the jet apex at higher frequencies, until the point where either the launching point is reached near the horizon, or particle acceleration has not yet begun²¹. The scale of a jet ‘nozzle’ emission cannot be smaller than the $\sqrt{27} r_g$ photon capture radius (Methods 1.4.5).

The combination of all emission regions along the jet gives rise to a flat to inverted radio spectrum, peaking at a maximum frequency $\tilde{\nu}$, determined by the black hole mass M and accretion rate \dot{M} and scaling as $\tilde{\nu} \propto M^{-1} \dot{M}^{2/3} \propto M^{-1} F_r^{8/17} D^{16/17}$ ^{6,19,22}. Here, D is the distance of the black hole to the observer and F_r the observed radio flux density. These scaling relations follow from the assumption that the jet’s internal gas and magnetic pressures are linearly coupled to the accretion rate and maintain a fixed ratio along the jets. The proportionality constant between \dot{M} and F_r generally depends on the jet’s velocity, electron and magnetic energy densities, particle distribution spectrum, and inclination angle. Therefore, we are only able to make a first order estimates. It should further be noted that X-ray binary observations²³ have revealed a more complex relationship between $\tilde{\nu}$ and \dot{M} , where the innermost particle acceleration zone in the jet may not remain stationary and source-specific accretion disk parameters come into play. The same effects are expected to also influence $\tilde{\nu}$ in AGN, which substantiates the fact that only order of magnitude estimates can be provided for $\tilde{\nu}$. We assume the brightest features in our image to correspond to the radio cores at 230 GHz, which is discussed in Methods 1.5. Our assumption is affirmed by three consistent and independent measurements of $\tilde{\nu}$, but future spectral information is needed for a definitive confirmation. We show that $\tilde{\nu}$ lies in the THz regime for Cen A based on the core shift that we can determine from our image, scaling relations with the M 87 jet, and the spectral energy distribution of Cen A.

We take the distance from the brightest pixel in the image to the estimated position of the jet apex and obtain a core shift of $z_{\text{core}} = 32 \pm 11 \mu\text{as}$. Based on this distance and the uncertain inclination angle, we estimate that an observing frequency of $\tilde{\nu}_{\text{CenA}} \sim 10 - 60 \text{ THz}$ (Methods 1.4.5) will reach the base of the jet at the black hole innermost stable circular orbit (ISCO). A caveat is that we do not take the effect of the uncertain ambient medium into account in this simple picture.

Independently, we can use the above scaling relations to estimate the order of magnitude of $\tilde{\nu}_{\text{CenA}}$ by comparing the Cen A jet with M 87, which has $\tilde{\nu}_{\text{M87}} = 228 \text{ GHz}$ ^{24,25}. For the cm jet radio core, a flux density of $\sim 1 \text{ Jy}$ is measured for both sources^{3,26}, which yields $\dot{M}_{\text{CenA}} \sim 0.1 \dot{M}_{\text{M87}}$ for the accretion onto the black hole and therefore $\tilde{\nu}_{\text{CenA}} \sim 26 \tilde{\nu}_{\text{M87}} \approx 6 \text{ THz}$ (Methods 1.4.5), in agreement with our observations and the assumed position of the black hole at the jet apex within an order of magnitude. Based on comparable jet velocities ($\sim 0.3c - 0.5c$) and

inclination angles ($\sim 20^\circ$), we have assumed the amount of Doppler boosting to be similar in both jets. The relation of accretion rates would constrain \dot{M}_{CenA} to be $\lesssim 9 \times 10^{-5} M_\odot \text{yr}^{-1}$ ²⁷ or $7 \times 10^{-5} \dot{M}_{\text{Edd}}$ in terms of the Eddington accretion rate for an assumed radiative efficiency of 10 %.

The core spectral energy distribution of Cen A peaks at $\sim 10^{13} \text{Hz}$ ²⁸, which may be the equivalent of the submillimeter bump seen in Sgr A*^{29,30}, and would further support our hypothesis.

Observed correlations between the masses of accreting black holes and their X-ray and radio luminosities form the basis of a unified fundamental plane of scale-invariant black hole accretion. This scale-invariance has been derived based on stellar-mass black holes, which have a break frequency $\tilde{\nu}_{\text{XRB}}$ in the near-infrared, and supermassive $10^8 M_\odot - 10^{10} M_\odot$ AGN, where $\tilde{\nu}_{\text{SMBH}}$ lies in the radio to submillimeter regime^{5,6}. With our observation, we demonstrate that the simple fundamental relations for the black hole jet activity still holds for a source with a mass of $5.5 \times 10^7 M_\odot$ and $\tilde{\nu}_{\text{CenA}}$ in the THz regime, in between those two types of black holes. Our method used to determine the optimal frequency to observe black hole shadows based on core shift, jet power, and source spectrum is in principle applicable to any LLAGN.

Our findings suggest that the black hole shadow⁴ of Cen A would be visible in a bright, optically thin accretion flow at an observing frequency of a few THz. At this high frequency, a VLBI experiment above the Earth's troposphere would be able to resolve the $1.4 \pm 0.8 \mu\text{as}$ shadow diameter with a minimal baseline length of $\sim 8000 \text{km}$.

References

- [1] Boccardi, B. , Krichbaum, T. P. , Ros, E. & Zensus, J. A. Radio observations of active galactic nuclei with mm-VLBI. *Astron. Astrophys. Rev.* **25**, 4 (2017).
- [2] Harris, G. L. H. , Rejkuba, M. & Harris, W. E. The Distance to NGC 5128 (Centaurus A). *Publ. Astron. Soc. Australia* **27**, 457-462 (2010).
- [3] Müller, C. et al. TANAMI monitoring of Centaurus A: The complex dynamics in the inner parsec of an extragalactic jet. *Astron. Astrophys.* **569**, A115 (2014).
- [4] Falcke, H. , Melia, F. & Agol, E. Viewing the Shadow of the Black Hole at the Galactic Center. *Astrophys. J. Letters* **528**, L13-L16 (2000).
- [5] Merloni, A. , Heinz, S. & di Matteo, T. A Fundamental Plane of black hole activity. *Mon. Not. R. Astron. Soc.* **345**, 1057-1076 (2003).
- [6] Falcke, H. , Körding, E. & Markoff, S. A scheme to unify low-power accreting black holes. Jet-dominated accretion flows and the radio/X-ray correlation. *Astron. Astrophys.* **414**, 895-903 (2004).
- [7] Neumayer, N. The Supermassive Black Hole at the Heart of Centaurus A: Revealed by the Kinematics of Gas and Stars. *Publ. Astron. Soc. Australia* **27**, 449-456 (2010).
- [8] Chatterjee, K. , Liska, M. , Tchekhovskoy, A. & Markoff, S. B. Accelerating AGN jets to parsec scales using general relativistic MHD simulations. *Mon. Not. R. Astron. Soc.* **490**, 2200-2218 (2019).
- [9] Janssen, M. et al. rPICARD: A CASA-based calibration pipeline for VLBI data. Calibration and imaging of 7 mm VLBA observations of the AGN jet in M 87. *Astron. Astrophys.* **626**, A75 (2019).
- [10] Blackburn, L. et al. EHT-HOPS Pipeline for Millimeter VLBI Data Reduction. *Astrophys. J.* **882**, 23 (2019).
- [11] Kim, J.-Y. et al. The limb-brightened jet of M87 down to the 7 Schwarzschild radii scale. *Astron. Astrophys.* **616**, A188 (2018).
- [12] Piner, B. G. , Pant, N. , Edwards, P. G. & Wiik, K. Significant Limb-Brightening in the Inner Parsec of Markarian 501. *Astrophys. J. Letters* **690**, L31-L34 (2009).
- [13] Giovannini, G. et al. A wide and collimated radio jet in 3C84 on the scale of a few hundred gravitational radii. *Nature Astronomy* **2**, 472-477 (2018).
- [14] Narayan, R. , Mahadevan, R. & Quataert, E. in *Theory of Black Hole Accretion Disks* (eds Abramowicz, M. A., Björnsson, G. & Pringle, J. E.) 148-182 (Cambridge Cont. Astrophys., 1998).

- [15] Blandford, R. D. & Payne, D. G. Hydromagnetic flows from accretion disks and the production of radio jets. *Mon. Not. R. Astron. Soc.* **199**, 883-903 (1982).
- [16] Blandford, R. D. & Znajek, R. L. Electromagnetic extraction of energy from Kerr black holes. *Mon. Not. R. Astron. Soc.* **179**, 433-456 (1977).
- [17] Gabuzda, D. Evidence for Helical Magnetic Fields Associated with AGN Jets and the Action of a Cosmic Battery. *Galaxies* **7**, 5 (2018).
- [18] Blandford, R. D. & Königl, A. Relativistic jets as compact radio sources. *Astrophys. J.* **232**, 34-48 (1979).
- [19] Falcke, H. & Biermann, P. L. The jet-disk symbiosis. I. Radio to X-ray emission models for quasars. *Astron. Astrophys.* **293**, 665-682 (1995).
- [20] Lobanov, A. P. Ultracompact jets in active galactic nuclei. *Astron. Astrophys.* **330**, 79-89 (1998).
- [21] Romero, G. E. , Boettcher, M. , Markoff, S. & Tavecchio, F. Relativistic Jets in Active Galactic Nuclei and Microquasars. *Space Sci. Rev.* **207**, 5-61 (2017).
- [22] Heinz, S. & Sunyaev, R. A. The non-linear dependence of flux on black hole mass and accretion rate in core-dominated jets. *Mon. Not. R. Astron. Soc.* **343**, L59-L64 (2003).
- [23] Lucchini, M. et al. Correlating spectral and timing properties in the evolving jet of the micro blazar MAXI J1836-194. *Mon. Not. R. Astron. Soc.* **501**, 5910–5926 (2020).
- [24] Hada, K. et al. An origin of the radio jet in M87 at the location of the central black hole. *Nature* **477**, 185-187 (2011).
- [25] Event Horizon Telescope Collaboration et al. First M87 Event Horizon Telescope Results. I. The Shadow of the Supermassive Black Hole. *Astrophys. J. Letters* **875**, L1 (2019).
- [26] Walker, R. C. , Hardee, P. E. , Davies, F. B. , Ly, C. & Junor, W. The Structure and Dynamics of the Subparsec Jet in M87 Based on 50 VLBA Observations over 17 Years at 43 GHz. *Astrophys. J.* **855**, 128 (2018).
- [27] Kuo, C. Y. et al. Measuring Mass Accretion Rate onto the Supermassive Black Hole in M87 Using Faraday Rotation Measure with the Submillimeter Array. *Astrophys. J. Letters* **783**, L33 (2014).
- [28] Abdo, A. A. et al. Fermi Large Area Telescope View of the Core of the Radio Galaxy Centaurus A. *Astrophys. J.* **719**, 1433-1444 (2010).
- [29] Falcke, H. et al. The Simultaneous Spectrum of Sagittarius A* from 20 Centimeters to 1 Millimeter and the Nature of the Millimeter Excess. *Astrophys. J.* **499**, 731-734 (1998).
- [30] Bower, G. C. et al. ALMA Observations of the Terahertz Spectrum of Sagittarius A*. *Astrophys. J. Letters* **881**, L2 (2019).
- [31] Ojha, R. et al. TANAMI: tracking active galactic nuclei with austral milliarcsecond interferometry . I. First-epoch 8.4 GHz images. *Astron. Astrophys.* **519**, A45 (2010).

Acknowledgments

The authors of the present paper thank the following organizations and programs: the Academy of Finland (projects 274477, 284495, 312496, 315721); the Agencia Nacional de Investigación y Desarrollo (ANID), Chile via NCN19_058 (TITANs) and Fondecyt 3190878; the Alexander von Humboldt Stiftung; an Alfred P. Sloan Research Fellowship; Allegro, the European ALMA Regional Centre node in the Netherlands, the NL astronomy research network NOVA and the astronomy institutes of the University of Amsterdam, Leiden University and Radboud University; the Black Hole Initiative at Harvard University, through a grant (60477) from the John Templeton Foundation; the China Scholarship Council; Consejo Nacional de Ciencia y Tecnología (CONACYT, Mexico, projects U0004-246083, U0004-259839, F0003-272050, M0037-279006, F0003-281692, 104497, 275201, 263356, 57265507); the Delaney Family via the Delaney Family John A. Wheeler Chair at Perimeter Institute; Dirección General de Asuntos del Personal Académico-Universidad Nacional Autónoma de México (DGAPA-UNAM, projects IN112417 and IN112820); the

EACOA Fellowship of the East Asia Core Observatories Association; the European Research Council Synergy Grant “BlackHoleCam: Imaging the Event Horizon of Black Holes” (grant 610058); the Generalitat Valenciana postdoctoral grant APOSTD/2018/177 and GenT Program (project CIDEAGENT/2018/021); MICINN Research Project PID2019-108995GB-C22; the Gordon and Betty Moore Foundation (grants GBMF- 3561, GBMF-5278); the Istituto Nazionale di Fisica Nucleare (INFN) sezione di Napoli, iniziative specifiche TEONGRAV; the International Max Planck Research School for Astronomy and Astrophysics at the Universities of Bonn and Cologne; Joint Princeton/Flatiron and Joint Columbia/Flatiron Postdoctoral Fellowships, research at the Flatiron Institute is supported by the Simons Foundation; the Japanese Government (Monbukagakusho: MEXT) Scholarship; the Japan Society for the Promotion of Science (JSPS) Grant-in-Aid for JSPS Research Fellowship (JP17J08829); the Key Research Program of Frontier Sciences, Chinese Academy of Sciences (CAS, grants QYZDJ-SSW-SLH057, QYZDJSSW- SYS008, ZDBS-LY-SLH011).

We further thank the Leverhulme Trust Early Career Research Fellowship; the Max-Planck-Gesellschaft (MPG); the Max Planck Partner Group of the MPG and the CAS; the MEXT/JSPS KAKENHI (grants 18KK0090, JP18K13594, JP18K03656, JP18H03721, 18K03709, 18H01245, JP19H01943, 25120007); the Malaysian Fundamental Research Grant Scheme (FRGS) FRGS/1/2019/STG02/UM/02/6; the MIT International Science and Technology Initiatives (MISTI) Funds; the Ministry of Science and Technology (MOST) of Taiwan (105- 2112-M-001-025-MY3, 106-2112-M-001-011, 106-2119- M-001-027, 107-2119-M-001-017, 107-2119-M-001-020, 107-2119-M-110-005, 108-2112-M-001-048, and 109-2124-M-001-005); the National Aeronautics and Space Administration (NASA, Fermi Guest Investigator grant 80NSSC20K1567, NASA Astrophysics Theory Program grant 80NSSC20K0527, NASA grant NNX17AL82G, and Hubble Fellowship grant HST-HF2-51431.001-A awarded by the Space Telescope Science Institute, which is operated by the Association of Universities for Research in Astronomy, Inc., for NASA, under contract NAS5-26555, and NASA NuSTAR award 80NSSC20K0645); the National Institute of Natural Sciences (NINS) of Japan; the National Key Research and Development Program of China (grant 2016YFA0400704, 2016YFA0400702); the National Science Foundation (NSF, grants AST-0096454, AST-0352953, AST-0521233, AST-0705062, AST-0905844, AST-0922984, AST-1126433, AST-1140030, DGE-1144085, AST-1207704, AST-1207730, AST-1207752, MRI-1228509, OPP-1248097, AST-1310896, AST-1337663, AST-1440254, AST-1555365, AST-1615796, AST-1715061, AST-1716327, AST-1716536, OISE-1743747, AST-1816420, AST-1903847, AST-1935980, AST-2034306); the Natural Science Foundation of China (grants 11573051, 11633006, 11650110427, 10625314, 11721303, 11725312, 11933007, 11991052, 11991053); a fellowship of China Postdoctoral Science Foundation (2020M671266); the Natural Sciences and Engineering Research Council of Canada (NSERC, including a Discovery Grant and the NSERC Alexander Graham Bell Canada Graduate Scholarships-Doctoral Program); the National Research Foundation of Korea (the Global PhD Fellowship Grant: grants 2014H1A2A1018695, NRF-2015H1A2A1033752, 2015- R1D1A1A01056807, the Korea Research Fellowship Program: NRF-2015H1D3A1066561, Basic Research Support Grant 2019R1F1A1059721); the Netherlands Organization for Scientific Research (NWO) VICI award (grant 639.043.513) and Spinoza Prize SPI 78-409; the New Scientific Frontiers with Precision Radio Interferometry Fellowship awarded by the South African Radio Astronomy Observatory (SARAO), which is a facility of the National Research Foundation (NRF), an agency of the Department of Science and Innovation (DSI) of South Africa; the South African Research Chairs Initiative of the Department of Science and Innovation and National Research Foundation; the Onsala Space Observatory (OSO) national infrastructure, for the provisioning of its facilities/observational support (OSO receives funding through the Swedish Research Council under grant 2017-00648) the Perimeter Institute for Theoretical Physics (research at Perimeter Institute is supported by the Government of Canada through the Department of Innovation, Science and Economic Development and by the Province of Ontario through the Ministry of Research, Innovation and Science); the Spanish Ministerio de Economía y Competitividad (grants PGC2018-098915-B-C21, AYA2016-80889-P, PID2019-108995GB-C21); the State Agency for Research of the Spanish MCIU through the “Center of Excellence Severo Ochoa” award for the Instituto de Astrofísica de Andalucía (SEV-2017- 0709); the Toray Science Foundation; the Consejería de Economía, Conocimiento, Empresas y Universidad of the Junta de Andalucía (grant P18-FR-1769), the Consejo Superior de Investigaciones Científicas (grant 2019AEP112); the US Department of Energy (USDOE) through the Los Alamos National Laboratory (operated by Triad National Security, LLC, for the National Nuclear Security Administration of the USDOE (Contract 89233218CNA000001); the European Union’s Horizon 2020 research and innovation programme under grant agreement No 730562 RadioNet; ALMA North America Development Fund; the Academia Sinica; Chandra TM6- 17006X and DD7-18089X; the GenT Program (Generalitat Valenciana) Project CIDEAGENT/2018/021.

This work used the Extreme Science and Engineering Discovery Environment (XSEDE), supported by NSF grant ACI-1548562, and CyVerse, supported by NSF grants DBI-0735191, DBI-1265383, and DBI-1743442. XSEDE Stampede2 resource at TACC was allocated through TG-AST170024 and TG-AST080026N. XSEDE JetStream

resource at PTI and TACC was allocated through AST170028. The simulations were performed in part on the SuperMUC cluster at the LRZ in Garching, on the LOEWE cluster in CSC in Frankfurt, and on the HazelHen cluster at the HLRS in Stuttgart. This research was enabled in part by support provided by Compute Ontario (<http://computeontario.ca>), Calcul Quebec (<http://www.calculquebec.ca>) and Compute Canada (<http://www.computeCanada.ca>). We thank the staff at the participating observatories, correlation centers, and institutions for their enthusiastic support.

This paper makes use of the following ALMA data: ADS/JAO.ALMA#2016.1.01198.V. ALMA is a partnership of the European Southern Observatory (ESO; Europe, representing its member states), NSF, and National Institutes of Natural Sciences of Japan, together with National Research Council (Canada), Ministry of Science and Technology (MOST; Taiwan), Academia Sinica Institute of Astronomy and Astrophysics (ASIAA; Taiwan), and Korea Astronomy and Space Science Institute (KASI; Republic of Korea), in cooperation with the Republic of Chile. The Joint ALMA Observatory is operated by ESO, Associated Universities, Inc. (AUI)/NRAO, and the National Astronomical Observatory of Japan (NAOJ). The NRAO is a facility of the NSF operated under cooperative agreement by AUI. APEX is a collaboration between the Max-Planck-Institut für Radioastronomie (Germany), ESO, and the Onsala Space Observatory (Sweden). The SMA is a joint project between the SAO and ASIAA and is funded by the Smithsonian Institution and the Academia Sinica. The JCMT is operated by the East Asian Observatory on behalf of the NAOJ, ASIAA, and KASI, as well as the Ministry of Finance of China, Chinese Academy of Sciences, and the National Key R&D Program (No. 2017YFA0402700) of China. Additional funding support for the JCMT is provided by the Science and Technologies Facility Council (UK) and participating universities in the UK and Canada. The LMT is a project operated by the Instituto Nacional de Astrófisica, Óptica, y Electrónica (Mexico) and the University of Massachusetts at Amherst (USA), with financial support from the Consejo Nacional de Ciencia y Tecnología and the National Science Foundation. The IRAM 30-m telescope on Pico Veleta, Spain is operated by IRAM and supported by CNRS (Centre National de la Recherche Scientifique, France), MPG (Max-Planck-Gesellschaft, Germany) and IGN (Instituto Geográfico Nacional, Spain). The SMT is operated by the Arizona Radio Observatory, a part of the Steward Observatory of the University of Arizona, with financial support of operations from the State of Arizona and financial support for instrumentation development from the NSF. The SPT is supported by the National Science Foundation through grant PLR- 1248097. Partial support is also provided by the NSF Physics Frontier Center grant PHY-1125897 to the Kavli Institute of Cosmological Physics at the University of Chicago, the Kavli Foundation and the Gordon and Betty Moore Foundation grant GBMF 947. The SPT hydrogen maser was provided on loan from the GLT, courtesy of ASIAA. The EHTC has received generous donations of FPGA chips from Xilinx Inc., under the Xilinx University Program. The EHTC has benefited from technology shared under open-source license by the Collaboration for Astronomy Signal Processing and Electronics Research (CASPER). The EHT project is grateful to T4Science and Microsemi for their assistance with Hydrogen Masers. This research has made use of NASA's Astrophysics Data System. We gratefully acknowledge the support provided by the extended staff of the ALMA, both from the inception of the ALMA Phasing Project through the observational campaigns of 2017 and 2018. We would like to thank A. Deller and W. Brisken for EHT-specific support with the use of DiFX. We acknowledge the significance that Maunakea, where the SMA and JCMT EHT stations are located, has for the indigenous Hawaiian people.

The grants listed above collectively fund the Event Horizon Telescope project.

Author contributions

K.A., L.B., C.-k.C., S.I., M.J., J.K., J.Y.K., T.P.K., J.L., E.L., D.P.M, V.R., K.L.J.R., I.V.B, and M.W. have worked on the calibration of the EHT data. K.A., K.L.B., A.C., J.L.G., S.I., M.J., M.D.J., C.N., D.W.P., F.R., and M.W. have worked on the image reconstruction. M.B., K.C., J.D., P.G.E., H.F, C.M.F, C.G., M.J., M.K., Y.M., A.M., S.M, E.R., and M.W. have worked on the interpretation of the results. M.J, M.K., C.M., and E.R. have coordinated the research. The Event Horizon Telescope collaboration as a whole has enabled this research by building the EHT instrument and producing the tools and knowledge for the reduction, analysis, and interpretation of the data.

Competing interests

The authors declare no competing interests.

Main text figures

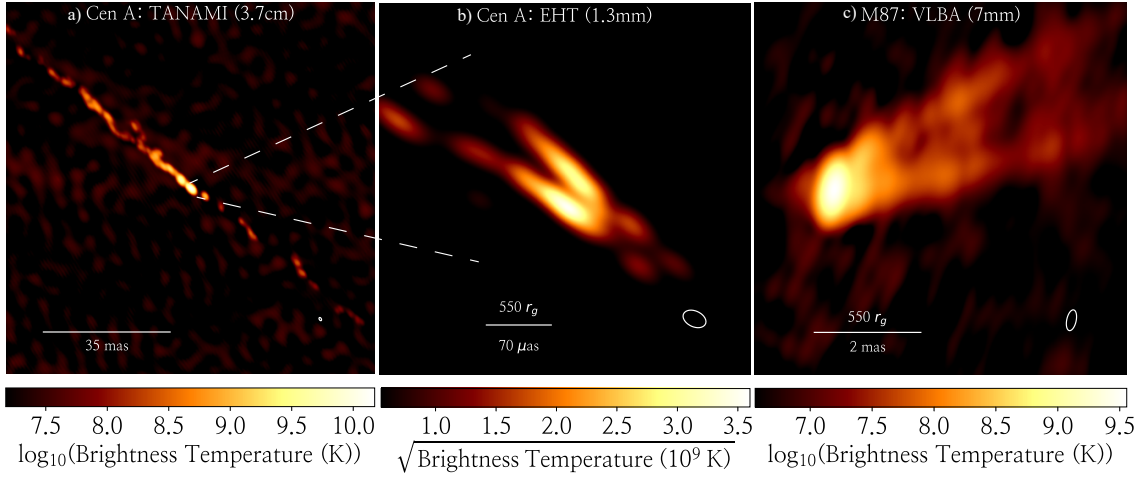


Figure 1: The jet structure of Cen A in comparison with M87. The left panel (a) shows the large scale jet of Cen A from an 8 GHz ($\lambda 3.7$ cm) TANAMI³¹ observation in November 2011³ on a logarithmic color scale. The middle panel (b) depicts our final EHT image from April 2017, blurred to the nominal resolution for a uniform weighting of the visibilities (the beams are shown in the bottom right corners). The reconstruction is based on the rPICARD data and is shown on a square-root scale, where values below a brightness temperature of 3×10^8 K are clipped, due to a lower dynamic range compared to the longer-wavelength observations. An unclipped and unconvolved version of this image is shown in Figure 2. The right panel (c) shows the M87 jet at 43 GHz ($\lambda 7$ mm) from a Very Long Baseline Array observation in June 2013^{9,26} on a logarithmic scale. North is up and east is to the left. The physical, linear scales of the full field of views shown in the three images are 2 parsec (pc) for TANAMI (left), 0.007 pc for the EHT (middle), and 0.6 pc for the VLBA (right).

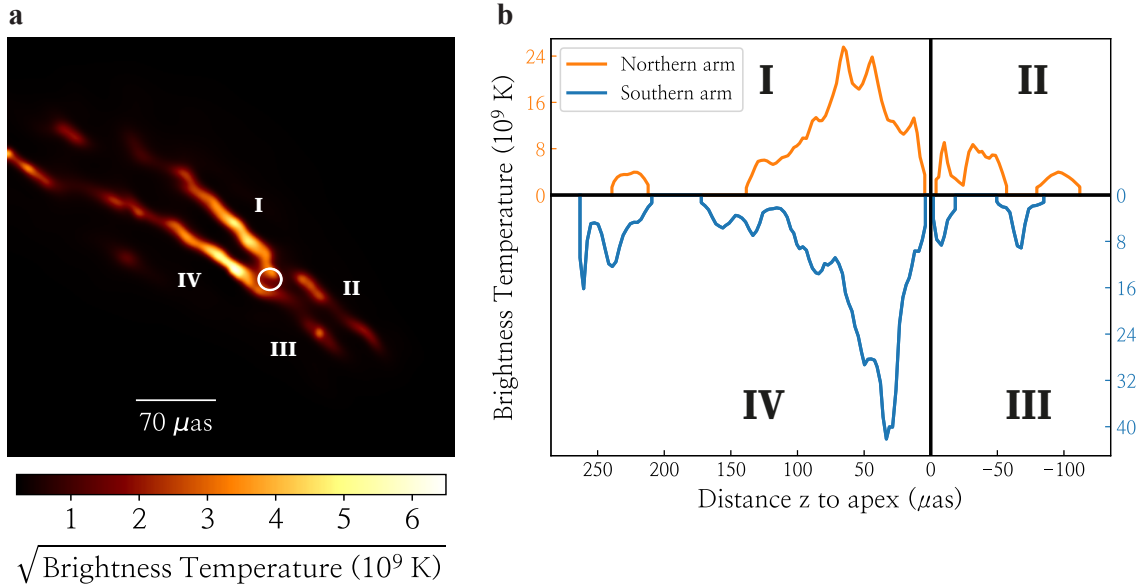


Figure 2: Image analysis of the final model. The model image shown in the left panel (a) corresponds to the image from Figure 1 with a pixel size of $2 \mu\text{as}$. Here, the tentative position of the jet apex is indicated with a circle. The size of the circle indicates the uncertainty in the apex location. The right panel (b) shows the central brightness temperatures along the jet ridgelines from the model in four quadrants as a function of distance to the jet apex. The quadrants I, II, III, and IV correspond to the similarly marked regions of the jet in the left panel. Negative values for the distance to the jet apex are assigned for the counterjet region. Brightness temperatures of the fainter NW (orange line) and brighter SE (blue line) arms are shown in the upper and lower panels, respectively.

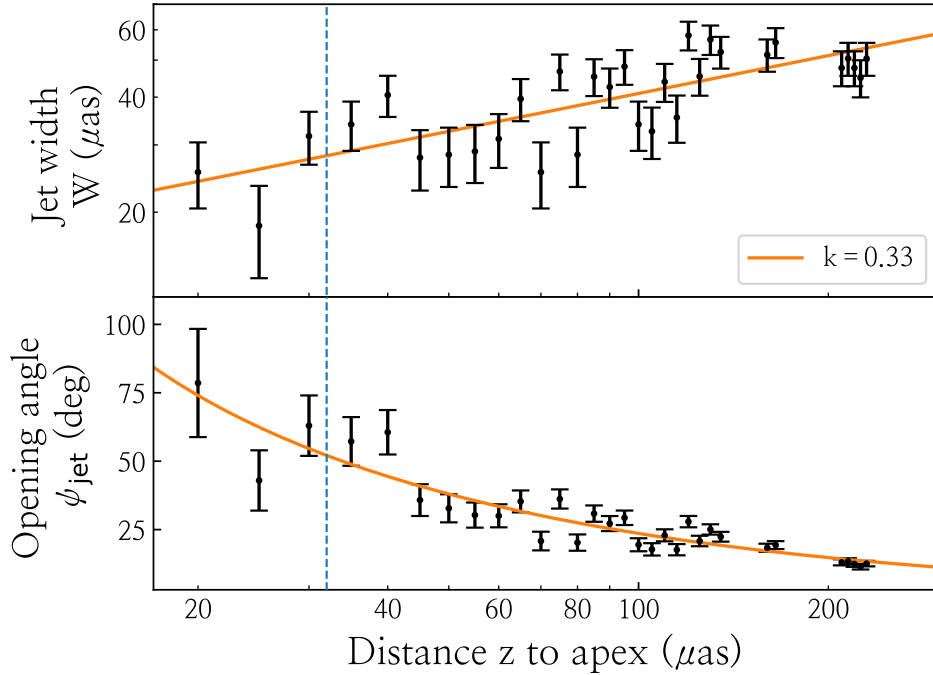


Figure 3: Cen A collimation profile derived from the final model. The top panel shows the jet width W as a function of apex distance z , overplotted with a $W(z) = Az^k$ least-squares fit, with $k = 0.33 \pm 0.05|_{\text{stat}} \pm 0.06|_{\text{sys}}$ (Methods 1.4.3). The systematic error has been derived based on the uncertainty in the apex position. The error bars are derived from a $5 \mu\text{as}$ one sigma statistical uncertainty on each pixel in the model. The bottom panel shows the corresponding jet opening angle between the apex and the two jet arms, which becomes unreliable at $z \lesssim z_{\text{col}} = 32 \mu\text{as}$ due to instrumental resolution limitations (see text). The transition region is indicated with a vertical blue dashed line. A base-10 logarithmic scale is used for the horizontal axis.

1 Methods

1.1 Processing of observational data

This section describes the 2017 EHT observations of Cen A, the model-independent calibration⁹ with two separate pipelines, the flux density calibration, and known measurement issues and systematics with corresponding mitigation strategies. The final data sets coming out from the two pipelines are both used for the scientific analysis as cross-verification (Supplementary Fig. 5).

1.1.1 Data acquisition

Cen A (PKS 1322–428, hosted in the NGC 5128 elliptical galaxy, $\alpha_{\text{J2000}} = 13^{\text{h}}25^{\text{m}}27.62^{\text{s}}$, $\delta_{\text{J2000}} = -43^{\circ}1'8.81''$) was observed by the EHT in a six hour long track on April 10 2017, with a total on-source integration time of 105 minutes (Supplementary Fig. 6). The observations were carried out by the Atacama Large Millimeter/submillimeter Array (ALMA), Atacama Pathfinder Experiment (APEX), James Clerk Maxwell Telescope (JCMT), Large Millimeter Telescope Alfonso Serrano (LMT), South Pole Telescope (SPT)³², Submillimeter Array (SMA), and Submillimeter Telescope (SMT)³³. For ALMA, 37 of the 12 m dishes were phased-up³⁴. The EHT IRAM 30 m Telescope is not able to see Cen A jointly with rest of the array due to the low declination of the source. The data were recorded on Mark 6 VLBI recorders³⁵ with 2-bit sampling in two 2 GHz wide bands, ‘low’ and ‘high’, centred around 227.1 GHz and 229.1 GHz, respectively. Unless stated otherwise, results are derived using the combined low+high band data. Quarter-wave plates at each site except ALMA were used to observe circularly polarized light. The data were correlated with the DiFX software^{36,37}. The PolConvert³⁸ software was used to convert the phased ALMA data³⁴ from a linear polarization basis to a circular basis after correlation, based on solutions from the calibration of the connected-element ALMA data³⁹.

1.1.2 Data reduction pipelines

The autocorrelation normalization, feed angle rotation, fringe fitting, bandpass calibration, and a priori correction of atmospheric phase turbulence⁴⁰ were performed independently by the CASA-based rPICARD^{9,41} and EHT-HOPS^{10,42} pipelines. DiFX produces FITS-IDI and Mark4 data. rPICARD uses the FITS-IDI product and converts it into the Measurement Set format. EHT-HOPS uses the Mark4 data. Both software packages convert the calibrated data into the UVFITS format for further processing.

rPICARD performs an upstream correction for the feed rotation angle and uses station-based global fringe fitting based on an unpolarized point source model to correct for phases, delays, and rates consistently for the right circular polarization and left circular polarization signal paths⁴³. Atmospheric phase and residual delay variations are corrected within the expected coherence time by fringe fitting segmented data of each VLBI scan. The segmentation length is set by the signal-to-noise ratio (S/N) of each baseline.

For EHT-HOPS, the feed rotation angle is corrected after the fringe-fitting together with an additional polarization calibration step, where complex R-L gain offsets are solved for. Delays and rates are found in a baseline-based fringe search and referenced to individual stations with a least-squares optimization⁴⁴. Atmospheric phases are corrected by fitting a polynomial phase model to the data on baselines to the most sensitive reference station in each scan. A round-robin approach is used to avoid fitting to thermal noise and the degree of the polynomial is set by the S/N of the data.

1.1.3 Gain amplitude calibration

The flux density calibration is done based on determined station sensitivities in a common framework for the rPICARD and EHT-HOPS data⁴⁵. The sensitivity of a station i is given by its system equivalent flux density (SEFD _{i}) in Jy, which takes into account the gain and total noise power along a telescope’s signal chain as a function of time t and frequency ν . On a baseline i – j , correlation coefficients $\xi_{(i,j)}$ in units of thermal noise are calibrated to a physical radiation intensity scale of correlated flux density $\mathcal{S}_{(i,j)}$ through

$$\mathcal{S}_{i,j}(t, \nu) = \frac{\sqrt{\text{SEFD}_i(t, \nu)\text{SEFD}_j(t, \nu)}}{\eta_Q} \xi_{i,j}(t, \nu), \quad (1)$$

where η_Q is the quantization efficiency. For data recorded with 2-bit sampling, we have $\eta_Q \approx 0.88$.

The gains of co-located stations were solved based on a contemporaneous measurement of the total flux density $S_0 = 5.62$ Jy of the source with the ALMA interferometer^{10,39,45}. The correlated flux \mathcal{S} measured between two co-located sites p and q should be equal to S_0 and for a third station o , we should have $\mathcal{S}_{po} = \mathcal{S}_{qo}$. It follows, that we can solve for the station-based amplitude gains \mathcal{A} of p and q with a self-calibration approach. Here, the model is given by the constant flux density S_0 seen by baselines between co-located sites. No gain corrections for non-co-located (‘isolated’) stations are solved for.

Ad hoc correction factors are used to correct signal losses at APEX due to an injected instrumental signal and at SMA due to temporary losses of bandwidth⁴⁵. Additionally, LMT and SPT suffered from pointing problems, which result in significant amplitude variations between and within VLBI scans. These losses cannot be estimated a priori and must be corrected with self-calibration gain solutions derived within short ~ 10 s segments from high S/N data. The SMT station was able to track the source down to an elevation of a few degrees. Large self-calibration gain factors are therefore needed towards the end of the experiment. Besides these known data issues, gain corrections factors are well constrained within a determined a priori error budget ranging between 10–20% for the individual stations⁴⁵.

1.2 Imaging

In this section, we describe how we obtained our image model from the observational data. In a first step, we have established a blind consensus between different imaging methods. Then, we have fine-tuned the parameters of one method, eht-imaging^{46,47}, for the rPICARD and EHT-HOPS data, to obtain final images for the analysis of the Cen A jet structure.

The highest resolution images of this southern source prior to this work were obtained within the TANAMI program³¹ at 8 and 22 GHz with a maximum resolution of $400 \mu\text{as}$, showing an extremely collimated structure with multiple distinct radio knot emission regions³. In a previous single-baseline non-imaging study of Cen A, a bright compact core was detected at 215 GHz⁴⁸.

1.2.1 Blind challenge

Similarly to the method used when the shadow of M87* was resolved by the EHT^{25,49}, we have carried out a *blind imaging challenge* before proceeding to the scientific analysis of the data. In this challenge, a number of individuals have reconstructed an image of the source independently of each other. Early (not fully verified) low band data from the EHT-HOPS pipeline was used, which had slightly larger amplitude gain errors from outdated a priori calibration parameters. Out of twelve total images, six had acceptable reduced $\chi_{\text{cp}}^2 < 2$ for the closure phases. These images were obtained with the eht-imaging and SMILI^{50,51} regularized maximum likelihood methods and the Difmap^{52,53} and CASA^{9,54} CLEAN methods^{55,56}. The images that did not make the χ^2 cut often showed spurious emission features and strong sidelobe structures.

1.2.2 Final imaging method

With the imaging challenge, we have established that different methods converge towards the same robust source structure (Supplementary Fig. 5), independent of shared human bias. Further imaging analysis of the rPICARD & EHT-HOPS science release data was pursued with the final M87* eht-imaging script⁴⁹, which is based on application of a regularized maximum likelihood method that includes a maximum-entropy term. Using a second-moment-based pre-calibration, LMT gains were stabilized with respect to the better constrained SMT amplitudes⁵⁷. As Cen A is sufficiently compact within the EHT beam, the short LMT–SMT baseline measures a Gaussian-like source structure. We have performed an initial self-calibration to a Gaussian with size $\Theta_{\text{maj}} \times \Theta_{\text{min}}$ at a position angle Θ_{PA} and with a total flux of S_G . Any gains that were erroneously introduced in this process can later be reconciled in image-based self-calibration steps. To solve for the image brightness distribution \mathcal{I} with a regularized maximum likelihood method (employed by eht-imaging), we are minimizing

$$\sum_D \alpha_D \chi_D^2(\mathcal{I}) - \sum_R \beta_R \Lambda_R(\mathcal{I}). \quad (2)$$

Here, D represents the collection of data terms, which are derived from the measured visibilities and have approximately normal noise statistics⁵⁸: amplitudes, closure phases, and log closure amplitudes. Corresponding to each data term, we have a goodness-of-fit function $\chi_D^2 = \{\chi_{\text{amp}}^2, \chi_{\text{cp}}^2, \chi_{\text{lca}}^2\}$ and relative weighting $\alpha_D = \{\alpha_{\text{amp}}, \alpha_{\text{cp}}, \alpha_{\text{lca}}\}$. We have performed four incremental imaging runs with subsequent self-calibration, over which we have increased the weight of each data term: $\alpha_D^{(1)} \rightarrow \alpha_D^{(2)} \rightarrow \alpha_D^{(3)}$ with $\alpha_D^{(1)} < \alpha_D^{(2)} < \alpha_D^{(3)} \forall D$. Regularizer terms Λ_R are included with weights β_R to impose additional assumptions on the image. We have imposed two regularization parameters: One for a maximum entropy method (MEM)⁵⁹ term with weight β_{MEM} and another one for the amount of compact flux Z_0 in the image with weight β_z . The MEM term minimizes the entropy of \mathcal{I} with respect to a prior image Φ , which results in a similarity between the two images for each pixel i . Here, we used $\Lambda_{\text{MEM}} = -S_0^{-1} \sum_i \mathcal{I}_i \log(\mathcal{I}_i/\Phi_i)$. For the MEM prior image Φ , we have chosen a Gaussian model oriented along the direction of the large-scale jet, which we also used as initialization for our imaging. It is expected that $Z_0 < S_0$, as a significant portion of the flux measured by ALMA may come from different emission mechanisms and larger scales outside of the EHT field of view. In fact, the ~ 150 m JCMT-SMA baseline sees a flux density of about 5 Jy and at 2 km, ALMA-APEX recovers only ~ 4 Jy. For M87*, the EHT measured $Z_0 \approx S_0/2$ ⁴⁹.

The numerical values of the final imaging parameters are given in the supplementary material (Table 1). Optimal parameters were chosen based on an empirical minimization of χ_D^2 , median station gains $\mathcal{A}^{(\text{sc})}$ from self-calibration, and patches of spurious flux in the image. Additionally, we took the similarity of image reconstructions from the rPICARD and EHT-HOPS data for a given set of parameters into account to avoid over-fitting to data peculiarities that result from assumptions made during the data calibration. A variety of images that can be reconstructed with various combinations of the free imaging parameters can be shared upon reasonable requests. We have chosen for an eht-imaging reconstruction of the rPICARD data for our final image, as this imaging method and data set have been studied most extensively.

Our images are shown in units of brightness temperature \mathcal{T} [K], which is related to a flux density S in Jy through the observing wavelength λ , Boltzmann constant k_B , and angular resolution element Ω as $\mathcal{T} = \lambda^2 (2k_B\Omega)^{-1} S$.

Fundamental data properties and fits of the final image model to the data are shown in Supplementary Fig. 7. In Supplementary Fig. 8, we show the measured amplitudes projected along and perpendicular to the jet PA. Along the jet axis, amplitudes fall off quickly at long projected baseline lengths, indicating the absence of substructures along the jet. Perpendicular to the jet, ‘bouncing’ amplitudes out to large projected baseline lengths occur, due to the strong intensity gradients across the transverse jet profile.

1.3 Synthetic data imaging tests

We have used the SYMBA software⁶⁰ to perform imaging studies based on simulated observations. Given an input source model \mathcal{M} , SYMBA follows the entire EHT signal path to predict which source structure \mathcal{I} would eventually be reconstructed. Thereby, we can assess how close our image reconstruction comes to the ground truth structure \mathcal{M} of a fabricated observed source. SYMBA simulates the parameters of the Earth’s atmosphere with the ATM module⁶¹ to add sky noise, signal attenuation, and phase turbulence. Next, gain, leakage, pointing, and focus errors plus thermal noise are introduced for each telescope in the array based on known telescope properties⁶². Afterwards, the simulated corrupted data are calibrated by rPICARD in the same way as observational data. The u, v coverage and SEFD sensitivities are taken from the 2017 Cen A EHT observation track. The simulated calibrated data are then imaged with the same final eht-imaging script used to image the observational data in this work.

To assess the robustness of secondary features in our image reconstruction, we have performed three synthetic data tests (Supplementary Fig. 4). Firstly, a control study to demonstrate that the output reconstruction from SYMBA correctly matches the input model $\mathcal{M}_{\text{final}}$. Then, we have removed the counterjet and emission features at large distance to the apex z from $\mathcal{M}_{\text{final}}$ to verify that these do not spuriously appear in our simulated observation.

Furthermore, we have explored the upper limit on the brightness \mathcal{T}_{sp} of potential emission from the jet spine by adding a weak emission component in the central jet region to $\mathcal{M}_{\text{final}}$. The goal was to find the smallest \mathcal{T}_{sp} , which would still be registered as an emission region in the reconstructed image $\mathcal{I}(\mathcal{M}_{\text{final}} + \mathcal{T}_{\text{sp}})$.

1.4 Jet structure analysis

This section describes how we extract fundamental jet parameters from our image based on geometric arguments.

1.4.1 The position of the jet apex

We can empirically determine the approximate position of the jet apex, where the jet and counterjet are being launched, from the high resolution image model shown in Figure 2. A zoomed-in version of this plot is shown in Supplementary Fig. 9, which is overlaid with visual aids for the determination of the apex location. The first consideration is that the apex should be located in the region where the streamlines of the approaching jet converge. In our image, this convergence region lies upstream of the optically thick radio cores (assumed to correspond to the brightest regions of the jet) for both the NW and SE jet arms. Here, we are limited by the resolution of our instrument, but a tentative merge of the two arms can be seen. The upper arm (region I in the figure) exhibits a strong bend, while the lower arm (IV) remains mostly straight. We note that a similar structure, where one jet arm appears to be straighter than the other one is also present in the M87 jet²⁶. The second consideration is the symmetry between the approaching jet and the counterjet. We note that there is no clear correspondence between individual features in the jet and counterjet. The counterjet appears straight with two components in the upper region (II) and one component in the lower region (III). As the apex must be upstream of the counterjet, the closest component of the receding jet to the approaching jet constrains how far upstream of the approaching jet the apex position can be. In fact, the position we assume for the apex based on the first consideration, where the streamlines of the approaching jet converge, lies halfway between the radio core in region I and the closest counterjet component in region II. It should be noted that a simple extrapolation of only the edge-brightened approaching jet would place the apex well inside the faint counterjet region.

Based on the robustness of our image reconstructions with different data sets, software packages, and imaging parameters, we assume a positional uncertainty of $5 \mu\text{as}$ for the robust features of the image model, which is in agreement with the width of the jet ridgelines. Taking all constraints on the apex location into account, we estimate an uncertainty of $10 \mu\text{as}$ on the position.

For the determination of z_{core} , the pixel and jet apex position uncertainties are added in quadrature. Based on possible jet apex positions within the estimated uncertainty, we fit the $W \propto z^k$ jet profile multiple times and derive a systematic error of ± 0.06 on k . When we used image model convolved with the nominal resolving beam, we obtain $k = 0.35$ with a statistical error of ± 0.2 .

1.4.2 Brightness asymmetries

The jet-counterjet asymmetry is most likely caused by relativistic boosting. We can calculate the $\mathcal{R}_{\text{j/cj}}$ brightness ratio by taking the average image flux density within $50 \times 100 \mu\text{as}$ rectangular regions on opposite sides of the apex. This ratio has to be interpreted with care, since the two regions may be at different distances to the jet apex. Moreover, counterjet radiation may be absorbed by the accretion flow and intrinsic jet-counterjet differences may arise from asymmetries in the jet launching process and the ambient medium^{63,64}.

If we assume the intrinsic emissivity to be the same in the jet sheath and spine, beaming effects can be invoked to explain observed differences in brightness across the jet. We note that the intrinsic emissivity of the jet sheath is likely larger than that of the spine, as mentioned in the main body of this work. The simplifying assumption of identical intrinsic emissivities can nonetheless be used to derive straightforward estimates for jet velocity components and the inclination angle θ , since Doppler boosting is expected to have a considerable contribution to the observed source structure. If the inclination angle θ is not too small, a significant portion of the spine emission may be beamed away from the line of sight. If the sheath and spine velocities are $c\beta_{\text{sh}}$ and $c\beta_{\text{sp}}$, respectively, the ratio of I_{sh} sheath and I_{sp} spine intensities in a continuous jet follows as

$$\mathcal{R}_{\text{sh/sp}} \equiv \frac{I_{\text{sh}}}{I_{\text{sp}}} = \left[\frac{\sqrt{1 - \beta_{\text{sh}}^2} (1 - \beta_{\text{sp}} \cos(\theta))}{\sqrt{1 - \beta_{\text{sp}}^2} (1 - \beta_{\text{sh}} \cos(\theta))} \right]^{2-\alpha}, \quad (3)$$

with α ($I \propto \nu^\alpha$) as the spectral index of the optically thin jet components. Assuming a typical spectral index of $\alpha = -0.7$ and identical intrinsic emissivities, we can constrain the sheath and spine velocities with Equation 3 and $\mathcal{R}_{\text{sh/sp}} > 5$ to

$$(1 - \beta_{\text{sp}}^2)^{-0.5} (1 - \beta_{\text{sp}} \cos(\theta)) \gtrsim 1.8 (1 - \beta_{\text{sh}}^2)^{-0.5} (1 - \beta_{\text{sh}} \cos(\theta)). \quad (4)$$

$(1 - \beta^2)^{-0.5} (1 - \beta \cos(\theta))$ has a minimum of $\sqrt{1 - \cos^2(\theta)}$ at $\beta = \cos(\theta)$. It follows that the sheath-spine asymmetry can only be explained via beaming for $\beta_{\text{sp}} > \cos(\theta)$, independent of the assumed value for the spectral index.

For Cen A, the jet spine emission may be beamed away from the line of sight, when its velocity exceeds $0.7c - 0.9c$, while the sheath moves with a slower velocity. In fact, the emitting plasma of the large-scale jet was observed to move with $0.24c - 0.37c$ ³.

For a full three-dimensional picture of a jet, where we assume the sheath to be symmetric in the ϕ direction around the spine in a cylindrical coordinate system, different spine and sheath emissivities, due to beaming or intrinsic effects, cannot, on their own, explain edge-brightening. The reason is that the sheath emission will contribute to any sightline towards the jet. A more detailed description, where also the optical depth is taken into account, is given in the next paragraph. In the remainder of this section, we go through the different scenarios that could cause the observed edge-brightening. First, we discuss a common interpretation related to pathlength differences. As this only works in optically thin regions, we put the presence of helical magnetic fields forward as the most likely, intrinsic explanation for edge-brightening in LLAGN. We then discuss more exotic scenarios, of a rotating or asymmetric jet, which might be tested through future observations.

In the optically thin jet regions, the integrated column density along sightlines through the jet at different distances from its axis (center vs. edges) can be used to explain edge-brightening. These are sightlines that, across the transverse extent of the jet, enter the jet at different locations. The sightlines first pass through the near side of the jet and exit again at the other side of the jet, the far side. If we assume the absence of intrinsic spine emissivity (due to weak mass-loading or beaming of radiation into a narrow cone away from the line of sight), the observed radiation will be produced by a sheath of thickness ΔR . For a line sight that goes exactly through the center of the jet, we pass twice through the sheath, which would amount to a pathlength of $2\Delta R / \sin \theta$, when the pathlength is short enough to locally approximate the jet as a cylinder. For a local jet radius R_j , the column density along a sightline through the edge of the jet will be larger by a factor of $\sim \sqrt{R_j / \Delta R}$ ²⁶. Here, we have neglected changes in emissivity as sightlines pass through material at different distances to the jet apex. This simple model is capable of explaining edge-brightening in optically thin jet regions, where radiation along longer pathlengths accumulates. For Cen A, this would imply a thin radiating sheath with $\Delta R < 0.04R_j$.

However, the edge-brightening in Cen A extends to the presumably optically thick radio core, suggesting that different physics are at play in this jet. The likely presence of a helical magnetic field^{17,65,66,67} combined with a rotating sheath and the inclination angle θ , can lead to favorable/unfavorable pitch angles that maximize/minimize the synchrotron emissivity along the edges/center of the jet. For a power-law distribution of electrons, where in the rest-frame of the jet, the electron density n follows their energy E as $dn \propto E^{-p} dE$, the synchrotron emission coefficient in the rest frame scales as $j_\nu \propto |B \sin \chi|^{(p+1)/2} \nu^{-(p-1)/2}$ ^{68,69}. Here, B is the magnetic field strength, χ is the angle between the magnetic field and line of sight, and ν is the radiation frequency. The corresponding absorption coefficients scale as $\alpha_\nu \propto |B \sin \chi|^{(p+2)/2} \nu^{-(p+4)/2}$ ^{68,69}. It can be seen that no asymmetries in χ would arise across the transverse jet profile for a purely poloidal (B_z) magnetic field. The edge-brightening is maximized for perpendicular angles χ between the line of sight and magnetic field at the jet edges, while the magnetic field is oriented parallel to the line of sight in the center of the jet. In future work, we will study the polarimetric properties of the jet with the EHT to test this hypothesis as explanation for the edge-brightening. To get a handle on χ ,

it will be necessary to narrow down the inclination angle θ and jet velocity with monitoring observations to take relativistic aberration into account.

For optically thick jet regions upstream of the radio core, the relativistic boosting is sensitive to the shape of the emitting region and less sensitive to the Doppler factor¹⁸. In the presence of a fast helical jet flow and $\theta > 0$, part of the jet will rotate towards the observer and the other part will rotate in the opposite direction on the sky. Beyond the initial jet launching region, the jet is strongly collimated and the viewing angle to the jet edges will be very close to θ . For a flow with toroidal and poloidal components, we denote the angle of the helical velocity component β_h with respect to the poloidal direction along the line of sight with ϕ_h . For two identically shaped, optically thick radio core components of intensity I_s at the SE jet edge and I_n at the NW edge, we thus have²⁶

$$\mathcal{R}_{s/n} \equiv \frac{I_s}{I_n} = \left[\frac{1 - \beta_h \cos(\theta + \phi_h)}{1 - \beta_h \cos(\theta - \phi_h)} \right]^2. \quad (5)$$

For a counter-clockwise jet rotation and $\mathcal{R}_{s/n} \sim 1.6$, we get the weak constraint of

$$1.3 \cos(\theta - \phi_h) - \cos(\theta + \phi_h) \simeq 0.3\beta_h^{-1}. \quad (6)$$

When the bulk velocities of the NW and SE jet sheaths are known, ϕ_h and subsequently β_h can be determined²⁶. We note that the small linear scales resolved by the EHT in Cen A uniquely allow us to track relativistic dynamics across days in this source with future observations.

In an alternative scenario, this tentative NW-SE brightness asymmetry seen in Cen A could be explained with two distinct jet components having different velocities or different inclinations angles with respect to the line of sight.

In this work, we have interpreted the edge-brightening in terms of a naturally emerging spine-sheath jet structure in LLAGN, based on results from GRMHD simulations that are applicable to those type of sources. However, the same phenomenon is also observed in more powerful AGN; for example Cygnus A^{70,71}, where an accretion flow operating at $\sim 1\%$ of the Eddington limit is unlikely to be radiatively inefficient⁷².

1.4.3 Collimation profile

Following the NW and SE jet ridgelines, we bin distance values to the jet apex into intervals of $10 \mu\text{as}$ in size. Within each bin, we select the brightest pixel to obtain the central location along the ridge. We impose a statistical uncertainty of $5 \mu\text{as}$ on distances z in accordance with the width of the jet ridgelines in our image model. The width W of the jet is taken as the distance between the two jet arms. The profile of our image is shown in Figure 3 together with the corresponding average opening angle computed from the jet width as a function of distance to the apex.

Resolution limitations prevent us from tracing down the exact value of the initial jet opening angle ψ_{jet} near the apex, where the analysis of binned distance values becomes uncertain. Nonetheless, we can derive an upper limit on ψ_{jet} with a simple geometric argument: The jet has a clearly defined collimation region beyond some distance from the apex, at $z > z_{\text{col}}$. To estimate z_{col} , we have used the SE jet arm, as it is brighter, straighter, and has a more clearly identifiable compact brightness core. If we now assume that the jet stream converges monotonically towards the apex for $z < z_{\text{col}}$ and that the apex itself does not correspond to an extended region, we have

$$\psi_{\text{jet}} \geq 2 \arctan \left(\frac{W(z_{\text{col}})}{2z_{\text{col}}} \right). \quad (7)$$

If the inclination angle θ is known, the intrinsic opening angle ψ_{int} can be computed as⁷³

$$\psi_{\text{int}} \geq 2 \arctan \left(\sin(\theta) \frac{W(z_{\text{col}})}{2z_{\text{col}}} \right) = 2 \arctan \left(\sin(\theta) \tan \left(\frac{\psi_{\text{jet}}}{2} \right) \right). \quad (8)$$

The jet remains collimated out to kpc scales and contains multiple particle acceleration sites in a knotted structure^{3,74,75,76}. The source is a well-suited laboratory for models of AGN feedback^{77,78} and the creation of ultra-high-energy cosmic rays^{79,80}.

1.4.4 Confinement by the ambient medium

Analytic theory for axisymmetric, relativistic, poynting-dominated outflows can be used to derive exact asymptotic solutions for the influence an ambient medium on the collimation of a jet. One can show that in the presence of

external pressure gradient $P_{\text{ext}}(z) = P_0 z^{-\kappa}$, the jet expansion profile W as a function of distance along the jet axis z follows^{81,82}

$$\frac{d^2 W}{dz^2} - W^{-3} + C_1 P_0 z^{-\kappa} W = 0, \quad (9)$$

in a simplified form, with C_1 a numerical constant. At large z and for a shallow external pressure gradient with $\kappa < 2$, we obtain^{81,82}

$$W(z) = C_1^{-1/4} \sqrt{\frac{2-\kappa}{\pi}} \sqrt{C_2^{-1} \cos^2 S + C_2 \left(C_3 \cos S + \frac{\pi}{2-\kappa} \sin S \right)} z^{\kappa/4}, \quad (10)$$

for $S(z) = C_4 z^{1-\kappa/2} - C_5$ and C_2, C_3, C_4 , and C_5 numerical constants. Equation 10 shows that the ambient pressure will confine the jet into a $W \propto z^k$ profile with $k = \kappa/4$. Additionally, oscillations along the jet boundary can occur in a non-equilibrium state for $C_2 \neq (2-\kappa)/\pi$, $C_3 \neq 0$ ⁸².

1.4.5 The location of the black hole

Given a measurement of the core shift z_{core} with respect to the black hole, we can gauge the observing frequency $\tilde{\nu}$, which corresponds to a small self-absorbed nozzle region at the footprint of the jet⁸³. This region corresponds to a peak or break from a jet-dominated flat radio spectrum as it is the smallest region where particle acceleration can occur. The minimum scale where a jet can be launched by a black hole is given by the ISCO. The size of the emission region of this nozzle would be given by the photon capture radius. Thus, we can estimate $\tilde{\nu}$ as

$$\tilde{\nu} = \frac{\nu_{\text{obs}} z_{\text{core}}(\nu_{\text{obs}})}{\sqrt{27} r_g} \simeq 20 \left(\frac{\nu_{\text{obs}}}{\text{GHz}} \right) \left(\frac{z_{\text{core}}(\nu_{\text{obs}})}{\mu\text{as}} \right) \left(\frac{D}{\text{Mpc}} \right) \left(\frac{M}{10^6 M_\odot} \right)^{-1} \text{ GHz}. \quad (11)$$

In this expression, M is the mass of the black hole and D the distance from the black hole to the observer.

With the derived scaling relation of $\tilde{\nu} \propto M^{-1} \dot{M}^{2/3} \propto M^{-1} F_r^{8/17} D^{16/17}$, we can relate the break frequencies of two sources if their accretion rates or jet properties are known. Here, \dot{M} is the black hole accretion rate and F_r is the observed flat-spectrum radio flux density. In particular, if we assume for two sources to share the same basic intrinsic jet properties and orientation with respect to Earth, we have

$$\frac{\tilde{\nu}_1}{\tilde{\nu}_2} = \left(\frac{F_{r1}}{F_{r2}} \right)^{8/17} \left(\frac{D_1}{D_2} \right)^{16/17} \left(\frac{M_1}{M_2} \right)^{-1}. \quad (12)$$

While these expressions are strictly speaking only true for a filled conical jet, they appear to describe the emission from the jet sheath and its basic scaling properties reasonably well^{84,85,86} and allows one to make a first order estimate of the characteristic radio frequency of near-horizon emission.

We have used the above equations to estimate the accretion rate of Cen A to the one of M87 based on the assumption of a similar coupling between SMBH inflows and jet power. External Faraday Rotation effects and a generally variable rotation measure further complicates the assumed relation of accretion rates⁸⁷, which should thus be taken as only an order-of-magnitude estimate. It is however worth pointing out that the black hole growth rate measured over cosmic timescales from X-ray cavity fluxes from the jet radio lobes is $\sim 10^{-3} M_\odot \text{ yr}^{-1}$ for both Cen A and M87⁸⁸.

1.5 Alternative interpretations for the brightest jet features

In this work, we have interpreted the brightest jet features as radio cores, which mark the transition region between upstream synchrotron self-absorbed jet regions and downstream optically thin areas. In our image, we are able to resolve the self-absorbed region between the putative radio core and jet apex, which coincides with the location of the SMBH and its accretion disk. With current telescopes, the radio core and upstream region remains unresolved for most AGN (see Table 2 in¹ for example).

The radio core interpretation of the brightest jet features seems most plausible given our data. Based on simple analytical jet theory, a bright radio core is expected to be present in VLBI images. Radio cores are typically seen in sources similar to Cen A and the core-shift typically follows the standard ν^{-1} relation in most sources⁸⁹. In fact, special circumstances have to be invoked to explain the absence of radio cores in VLBI images. For example, obscuration by an optically thick region in the foreground. We do think that this is a likely scenario for our observation given the small scales probed in our image, the high observing frequency, and the proximity

of the source. Moreover, the core shift we have computed in Cen A agrees with the core SED of the source and fundamental plane equations that relate the jet power of Cen A to the M87 jet power. Our image is dominated by the brightest, compact jet features, which would be weakly polarized and have flat spectrum as radio cores¹. It should be noted that wide-bandwidth ALMA interferometer data, that were taken simultaneously with the VLBI observations, show a flat spectrum between 212 GHz and 230 GHz and place a 3σ upper limit of 0.15% on the linear polarization fraction⁸⁷. The ALMA measurements are however at a larger arcsecond resolution and we resolve out 64% of the flux measured by ALMA with the EHT. We therefore need future polarimetric and spectral VLBI results for confirmation.

However, with the current observations, we cannot conclusively rule out the possibility that there is insufficient particle acceleration in the jet, such that no radio core is formed at $\lambda 1.3$ mm, while a core is present at longer wavelengths^{3,76}. In this scenario, the bright jet regions would most likely correspond to a shock within the jet flow. The strongest counterargument here is that the radio spectrum of the core turns over at THz frequencies. This emission is most likely produced by the jet, ergo, particle acceleration should occur up to the energies that produce THz synchrotron emission.

2 Data availability

The ALMA raw visibility data can be retrieved from the [ALMA data portal](#) under the project code 2016.1.01198.V. The calibrated Stokes I VLBI visibility data of Centaurus A can be obtained from a DOI listed under <https://eventhorizontelescope.org/for-astronomers/data> with the code 2021-D03-01. Image FITS files and scripts to reproduce the plots are available from the corresponding author upon reasonable request.

3 Code availability

Antenna gains that enter the SEFDs were computed with https://bitbucket.org/M_Janssen/eht-flux-calibration. The SEFDs were applied with the <https://github.com/sao-eh/eat> code, which also contains the EHT-HOPS pipeline. rPICARD is hosted on https://bitbucket.org/M_Janssen/picard. Configuration and run files, which make use of self-contained Docker images are at https://bitbucket.org/M_Janssen/casaeht. This work is based on the ‘ER6’ data production scripts, for which the 30e6ca14fb50275013c668285a3b476f9bc85436.91da63236db34f3a31b5309b18ac159128f28a35 image was used.

The eht-imaging software is hosted on <https://github.com/achael/eht-imaging>. SYMBA is at https://bitbucket.org/M_Janssen/symba. The docker image used here is tagged as dec65699ccc0acdc6e6ba8f218d6724537fc613a and can be found on <https://hub.docker.com/r/mjanssen2308/symba>.

References

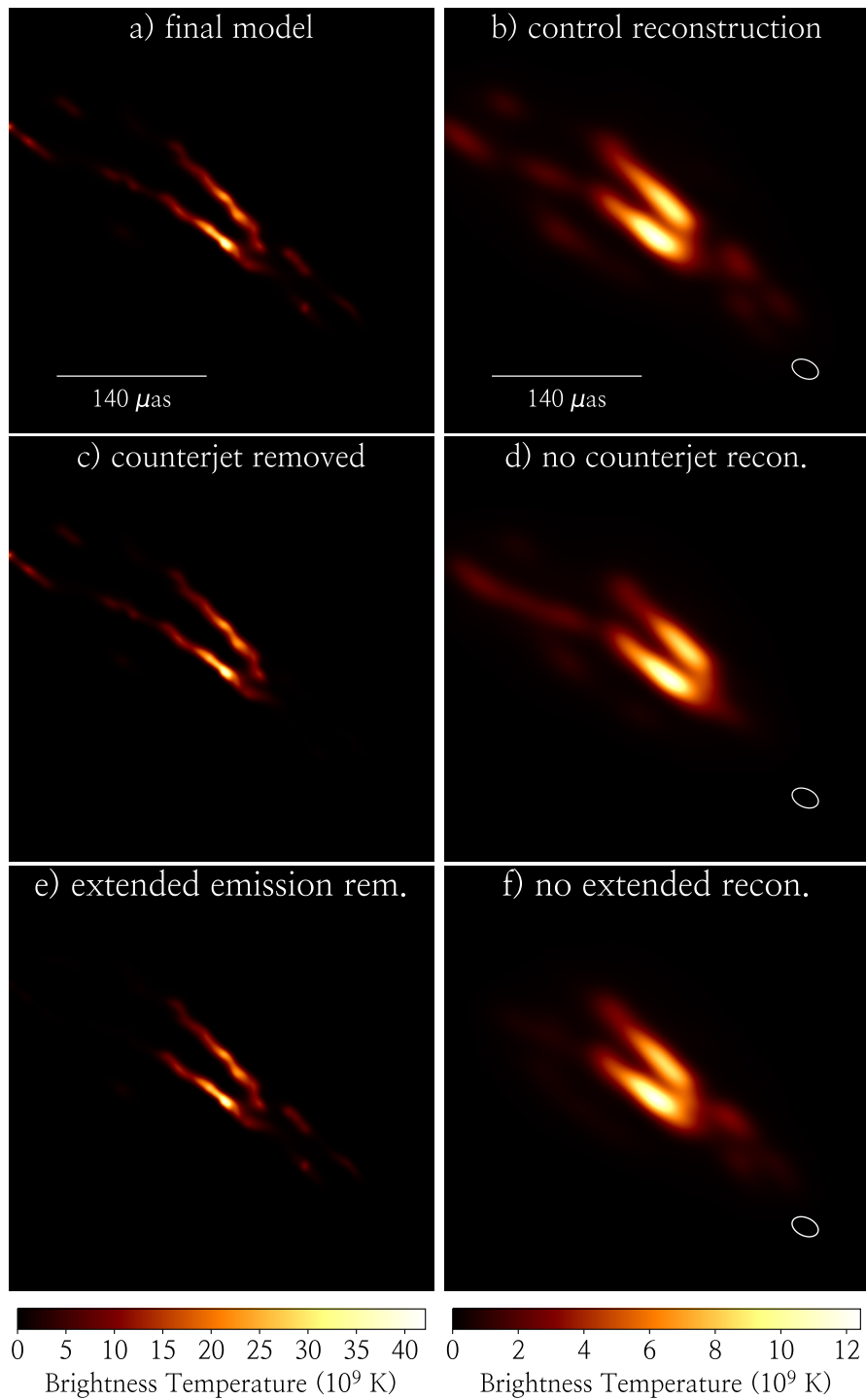
- [32] Kim, J. et al. A VLBI receiving system for the South Pole Telescope. *Proc. SPIE* **10708**, 107082S (2018).
- [33] Event Horizon Telescope Collaboration et al. First M87 Event Horizon Telescope Results. II. Array and Instrumentation. *Astrophys. J. Letters* **875**, L2 (2019).
- [34] Matthews, L. D. et al. The ALMA Phasing System: A Beamforming Capability for Ultra-high-resolution Science at (Sub)millimeter Wavelengths. *Pub. Astron. Soc. Pacific* **130**, 015002 (2018).
- [35] Whitney, A. R. et al. Demonstration of a 16 Gbps Station Broadband-RF VLBI System. *Pub. Astron. Soc. Pacific* **125**, 196 (2013).
- [36] Deller, A. T. , Tingay, S. J. , Bailes, M. & West, C. DiFX: A Software Correlator for Very Long Baseline Interferometry Using Multiprocessor Computing Environments. *Pub. Astron. Soc. Pacific* **119**, 318-336 (2007).
- [37] Deller, A. T. et al. DiFX-2: A More Flexible, Efficient, Robust, and Powerful Software Correlator. *Pub. Astron. Soc. Pacific* **123**, 275 (2011).
- [38] Martí-Vidal, I. , Roy, A. , Conway, J. & Zensus, A. J. Calibration of mixed-polarization interferometric observations. Tools for the reduction of interferometric data from elements with linear and circular polarization receivers. *Astron. Astrophys.* **587**, A143 (2016).

- [39] Goddi, C. et al. Calibration of ALMA as a Phased Array. ALMA Observations During the 2017 VLBI Campaign. *Pub. Astron. Soc. Pacific* **131**, 075003 (2019).
- [40] Thompson, A. R. , Moran, J. M. & Swenson, G. W. J. *Interferometry and Synthesis in Radio Astronomy, 3rd edn* (Springer, 2017).
- [41] Wootten, A. & Thompson, A. R. The Atacama Large Millimeter/Submillimeter Array. *IEEE Proceedings* **97**, 1463-1471 (2009).
- [42] W. A. R. et al. Mark 4 VLBI correlator: Architecture and algorithms. *Radio Science* **39**, RS1007 (2004).
- [43] Schwab, F. R. & Cotton, W. D. Global fringe search techniques for VLBI. *Astron. J.* **88**, 688-694 (1983).
- [44] Alef, W. & Porcas, R. W. VLBI fringe-fitting with antenna-based residuals. *Astron. Astrophys.* **168**, 365-368 (1986).
- [45] Event Horizon Telescope Collaboration et al. First M87 Event Horizon Telescope Results. III. Data Processing and Calibration. *Astrophys. J. Letters* **875**, L3 (2019).
- [46] Chael, A. A. et al. High-resolution Linear Polarimetric Imaging for the Event Horizon Telescope. *Astrophys. J.* **829**, 11 (2016).
- [47] Chael, A. A. et al. Interferometric Imaging Directly with Closure Phases and Closure Amplitudes. *Astrophys. J.* **857**, 23 (2018).
- [48] Kim, J. et al. The 1.4 mm Core of Centaurus A: First VLBI Results with the South Pole Telescope. *Astrophys. J.* **861**, 129 (2018).
- [49] Event Horizon Telescope Collaboration et al. First M87 Event Horizon Telescope Results. IV. Imaging the Central Supermassive Black Hole. *Astrophys. J. Letters* **875**, L4 (2019).
- [50] Akiyama, K. et al. Imaging the Schwarzschild-radius-scale Structure of M87 with the Event Horizon Telescope Using Sparse Modeling. *Astrophys. J.* **838**, 1 (2017).
- [51] Akiyama, K. et al. Superresolution Full-polarimetric Imaging for Radio Interferometry with Sparse Modeling. *Astron. J.* **153**, 159 (2017).
- [52] Shepherd, M. C. , Pearson, T. J. & Taylor, G. B. DIFMAP: an interactive program for synthesis imaging. *Bull. American Astron. Soc.* **26**, 987-989 (1994).
- [53] Shepherd, M. C. Difmap: an Interactive Program for Synthesis Imaging. *Astron. Soc. Pacific Conf* **125**, 77 (1997).
- [54] Rau, U. & Cornwell, T. J. A multi-scale multi-frequency deconvolution algorithm for synthesis imaging in radio interferometry. *Astron. Astrophys.* **532**, A71 (2011).
- [55] Högbom, J. A. Aperture Synthesis with a Non-Regular Distribution of Interferometer Baselines. *Astron. Astrophys. Supp.* **15**, 417 (1974).
- [56] Clark, B. G. An efficient implementation of the algorithm 'CLEAN'. *Astron. Astrophys.* **89**, 377 (1980).
- [57] Issaoun, S. et al. VLBI imaging of black holes via second moment regularization. *Astron. Astrophys.* **629**, A32 (2019).
- [58] Blackburn, L. et al. Closure Statistics in Interferometric Data. *Astrophys. J.* **894**, 31 (2020).
- [59] Narayan, R. & Nityananda, R. Maximum entropy image restoration in astronomy. *Ann. Rev. Astron. Astrophys* **24**, 127-170 (1986).
- [60] Roelofs, F. et al. SYMBA: An end-to-end VLBI synthetic data generation pipeline. *Astron. Astrophys.* **636**, A5 (2020).
- [61] Pardo, J. R. , Cernicharo, J. & Serabyn, E. Atmospheric transmission at microwaves (ATM): an improved model for millimeter/submillimeter applications. *IEEE Transactions on Antennas and Propagation* **49**, 1683-1694 (2001).

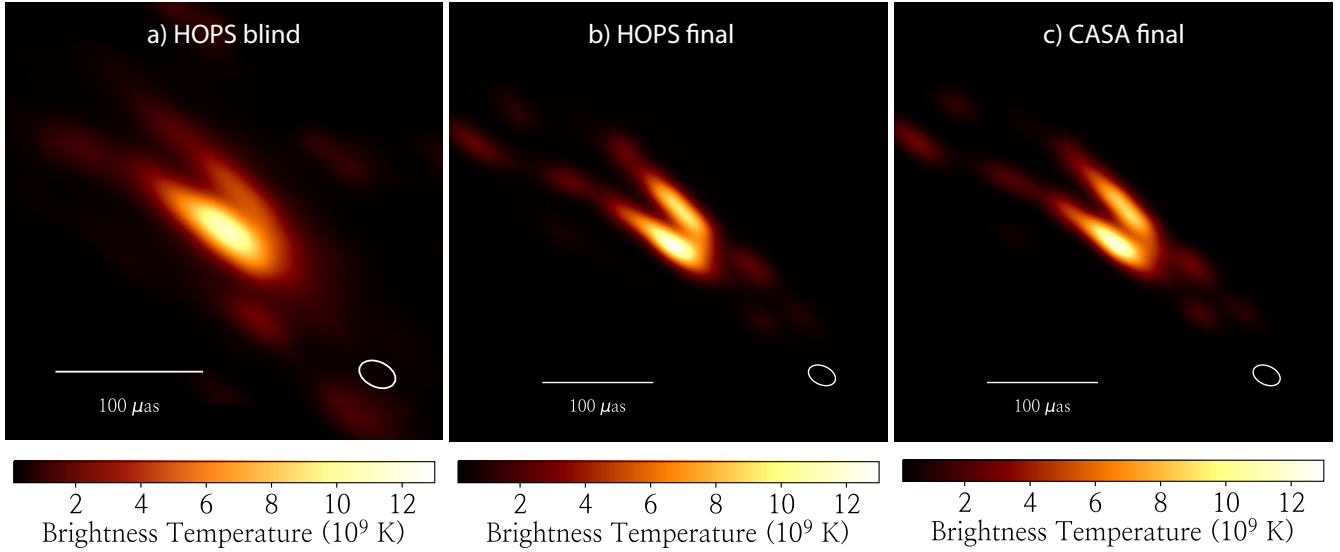
- [62] Blecher, T. , Deane, R. , Bernardi, G. & Smirnov, O. MEQSILHOUEETTE: a mm-VLBI observation and signal corruption simulator. *Mon. Not. R. Astron. Soc.* **464**, 143-151 (2017).
- [63] Baczkó, A.-K. et al. Asymmetric jet production in the active galactic nucleus of NGC 1052;ext-link ext-link-type. *Astron. Astrophys.* **623**, A27 (2019).
- [64] Nathanail, A. et al. Plasmoid formation in global GRMHD simulations and AGN flares. *Mon. Not. R. Astron. Soc.* **495**, 1549-1565 (2020).
- [65] Pushkarev, A. B. , Gabuzda, D. C. , Vetukhnovskaya, Y. N. & Yakimov, V. E. Spine-sheath polarization structures in four active galactic nuclei jets. *Mon. Not. R. Astron. Soc.* **356**, 859-871 (2005).
- [66] Hovatta, T. et al. MOJAVE: Monitoring of Jets in Active Galactic Nuclei with VLBA Experiments. VIII. Faraday Rotation in Parsec-scale AGN Jets. *Astron. J.* **144**, 105 (2012).
- [67] Gabuzda, D. C. , Nagle, M. & Roche, N. The jets of AGN as giant coaxial cables. *Astron. Astrophys.* **612**, A67 (2018).
- [68] Rybicki, G. B. & Lightman, A. P. *Radiative Processes in Astrophysics* (Wiley, 1979).
- [69] Clausen-Brown, E. , Lyutikov, M. & Kharb, P. Signatures of large-scale magnetic fields in active galactic nuclei jets: transverse asymmetries. *Mon. Not. R. Astron. Soc.* **415**, 2081-2092 (2011).
- [70] Boccardi, B. et al. The stratified two-sided jet of jASTROBJ_lCygnus A_l/ASTROBJ_l. Acceleration and collimation. *Astron. Astrophys.* **585**, A33 (2016).
- [71] Boccardi, B. , Krichbaum, T. P. , Bach, U. , Bremer, M. & Zensus, J. A. First 3 mm-VLBI imaging of the two-sided jet in Cygnus A. Zooming into the launching region. *Astron. Astrophys.* **588**, L9 (2016).
- [72] Tadhunter, C. et al. Spectroscopy of the near-nuclear regions of Cygnus A: estimating the mass of the super-massive black hole. *Mon. Not. R. Astron. Soc.* **342**, 861-875 (2003).
- [73] Pushkarev, A. B. , Kovalev, Y. Y. , Lister, M. L. & Savolainen, T. MOJAVE - XIV. Shapes and opening angles of AGN jets. *Mon. Not. R. Astron. Soc.* **468**, 4992-5003 (2017).
- [74] Israel, F. P. Centaurus A - NGC 5128. *Astron. Astrophys. Rev.* **8**, 237-278 (1998).
- [75] Hardcastle, M. J. et al. Radio and X-Ray Observations of the Jet in Centaurus A. *Astrophys. J.* **593**, 169-183 (2003).
- [76] Müller, C. et al. Dual-frequency VLBI study of Centaurus A on sub-parsec scales. The highest-resolution view of an extragalactic jet. *Astron. Astrophys.* **530**, L11 (2011).
- [77] Silk, J. & Rees, M. J. Quasars and galaxy formation. *Astron. Astrophys.* **331**, L1-L4 (1998).
- [78] Magorrian, J. et al. The Demography of Massive Dark Objects in Galaxy Centers. *Astron. J.* **115**, 2285-2305 (1998).
- [79] Pierre Auger Collaboration et al. An Indication of Anisotropy in Arrival Directions of Ultra-high-energy Cosmic Rays through Comparison to the Flux Pattern of Extragalactic Gamma-Ray Sources. *Astrophys. J. Letters* **853**, L29 (2018).
- [80] H.E.S.S. Collaboration et al. Resolving acceleration to very high energies along the jet of Centaurus A. *Nature* **582**, 356-359 (2020).
- [81] Komissarov, S. S. , Vlahakis, N. , Königl, A. & Barkov, M. V. Magnetic acceleration of ultrarelativistic jets in gamma-ray burst sources. *Mon. Not. R. Astron. Soc.* **394**, 1182-1212 (2009).
- [82] Lyubarsky, Y. Asymptotic Structure of Poynting-Dominated Jets. *Astrophys. J.* **698**, 1570-1589 (2009).
- [83] Falcke, H. , Mannheim, K. & Biermann, P. L. The Galactic Center radio jet. *Astron. Astrophys.* **278**, L1-L4 (1993).
- [84] McKinney, J. C. General relativistic magnetohydrodynamic simulations of the jet formation and large-scale propagation from black hole accretion systems. *Mon. Not. R. Astron. Soc.* **368**, 1561-1582 (2006).

- [85] Mościbrodzka, M. , Falcke, H. & Noble, S. Scale-invariant radio jets and varying black hole spin. *Astron. Astrophys.* **596**, A13 (2016).
- [86] Davelaar, J. et al. Modeling non-thermal emission from the jet-launching region of M 87 with adaptive mesh refinement. *Astron. Astrophys.* **632**, A2 (2019).
- [87] Goddi, C. , Martí-Vidal, I. , Messias, H. & et a. Polarimetric Properties of Event Horizon Telescope Targets from ALMA. *Astrophys. J. Letters* **910**, L14 (2021).
- [88] Rafferty, D. A. , McNamara, B. R. , Nulsen, P. E. J. & Wise, M. W. The Feedback-regulated Growth of Black Holes and Bulges through Gas Accretion and Starbursts in Cluster Central Dominant Galaxies. *Astrophys. J.* **652**, 216-231 (2006).
- [89] Sokolovsky, K. V. , Kovalev, Y. Y. , Pushkarev, A. B. & Lobanov, A. P. A VLBA survey of the core shift effect in AGN jets. I. Evidence of dominating synchrotron opacity. *Astron. Astrophys.* **532**, A38 (2011).

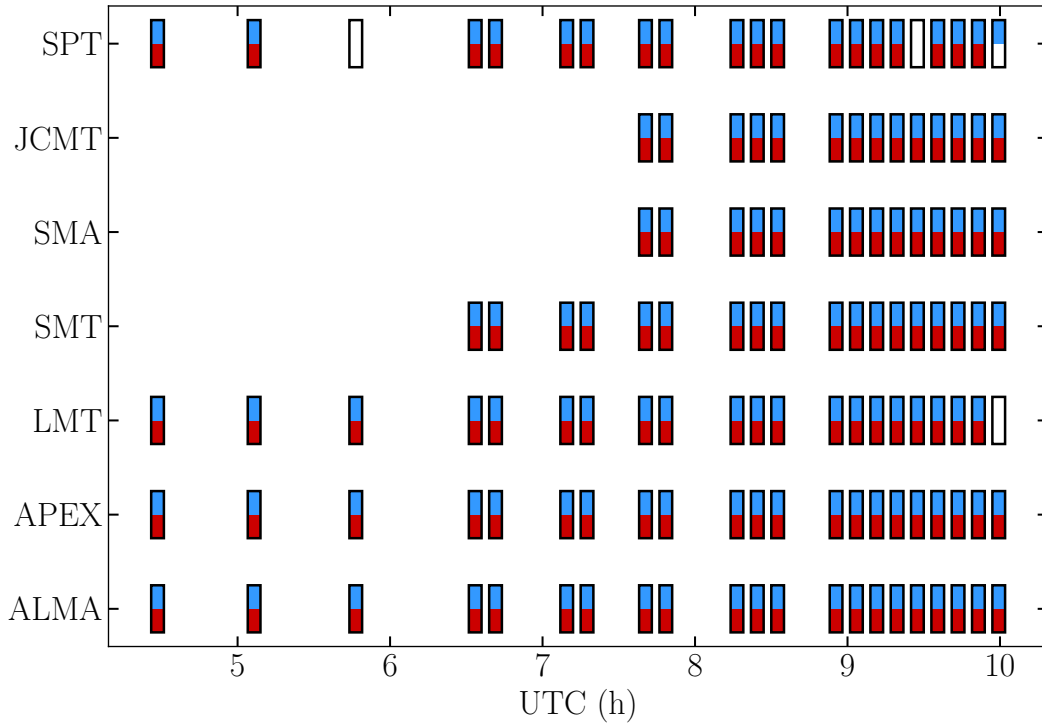
4 Supplement



Supplementary Figure 4: SYMBA synthetic data imaging tests. The left panel shows the input models \mathcal{M} , which are based on our observational image reconstruction. The corresponding reconstructions \mathcal{I} from the SYMBA pipeline are displayed in the right panel. (a-b) a control study, where the final model $\mathcal{M}_{\text{final}}$ underlying the image reconstruction $\mathcal{I}_{\text{final}}^{(\text{obs})}$ from the observational rPICARD data is passed through SYMBA. (c-d and e-f) same as (a-b) but the counterjet and extended jet emission features have been removed. The SYMBA reconstructions are convolved with a restoring beam, which matches the nominal resolution of the observation (shown in the bottom right corner).



Supplementary Figure 5: Image consistency across data sets. Left (a): Average image of six blind reconstructions from early EHT-HOPS low band (226–228 GHz) data, which was prepared with outdated a priori calibration parameters. Middle (b) and right (c): Images from the EHT-HOPS and rPICARD data, respectively, reconstructed with the final imaging parameters (Table 1). The restoring beams are plotted in the bottom right corner.

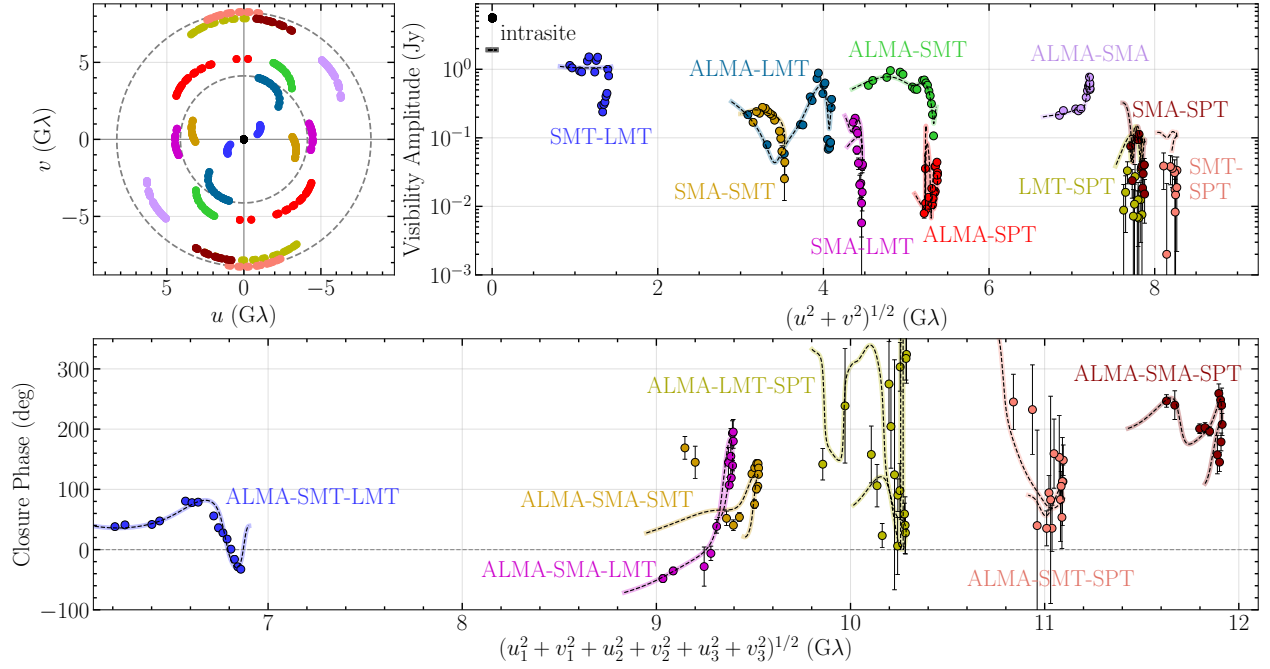


Supplementary Figure 6: Cen A observing block. The boxes show the planned VLBI scans in the observational VEX file. Blue (top) and red (bottom) markers in each box show detections in the EHT-HOPS and rPICARD data, respectively.

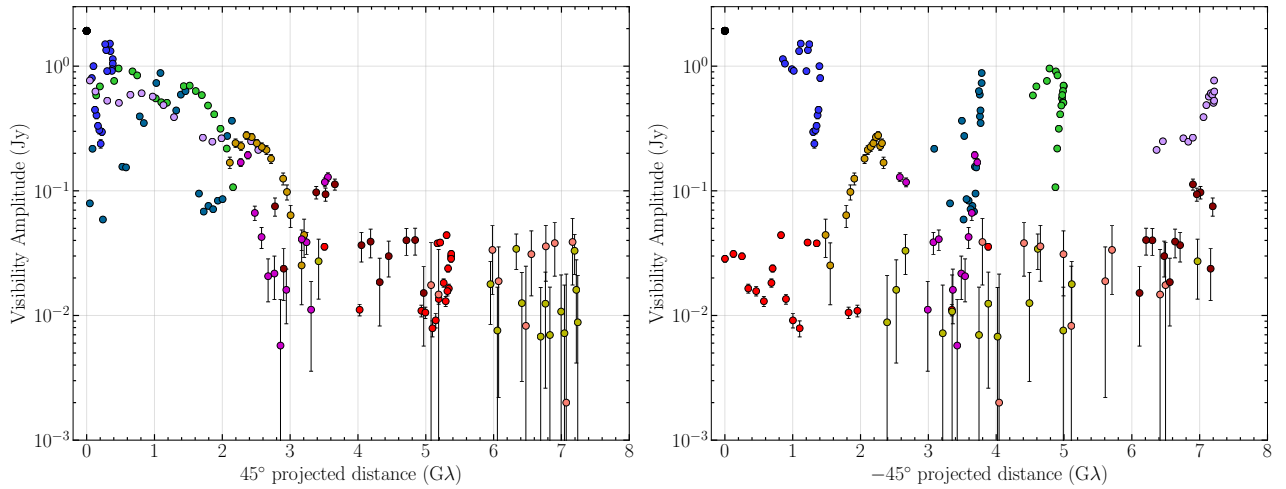
Supplementary Table 1: Final imaging parameters.

LMT Gaussian self-calibration	Θ_{maj}	major axis of Gaussian self-calibration model	$60 \mu\text{as}$
	Θ_{min}	minor axis of Gaussian self-calibration model	$60 \mu\text{as}$
	Θ_{PA}	position angle of Gaussian self-calibration model	0°
	S_G	flux density of Gaussian self-calibration model	0.6 Jy
Imaging priors	Φ_{maj}	major axis of Gaussian image prior	$70 \mu\text{as}$
	Φ_{min}	minor axis of Gaussian image prior	$18 \mu\text{as}$
	Φ_{PA}	position angle of Gaussian image prior	45°
	Z_0	flux density of Gaussian image prior	2 Jy
Regularizer weights	β_z	weight for Z_0	0.1
	β_{MEM}	weight for maximum entry minimization	10
Data weights	$\alpha_{\text{amp}}^{(1,2,3)}$	incremental weights for measured amplitudes	0.2, 2, 10
	$\alpha_{\text{cp}}^{(1,2,3)}$	incremental weights for measured closure phases	1, 10, 20
	$\alpha_{\text{lca}}^{(1,2,3)}$	incremental weights for measured log closure amplitudes	1, 10, 20
rPICARD image goodness of fit	χ_{amp}^2	goodness of fit for amplitudes	1.0
	χ_{cp}^2	goodness of fit for closure phases	1.8
	χ_{lca}^2	goodness of fit for log closure amplitudes	2.3
	$\mathcal{A}_{\text{intra}}^{(\text{sc})}$	mean self-calibration gain for co-located stations	0.98
	$\mathcal{A}_{\text{LMT}}^{(\text{sc})}$	LMT mean self-calibration gain	1.13
	$\mathcal{A}_{\text{SMT}}^{(\text{sc})}$	SMT mean self-calibration gain	1.01
	$\mathcal{A}_{\text{SPT}}^{(\text{sc})}$	SPT mean self-calibration gain	1.03
	EHT-HOPS image goodness of fit	χ_{amp}^2	goodness of fit for amplitudes
χ_{cp}^2		goodness of fit for closure phases	2.1
χ_{lca}^2		goodness of fit for log closure amplitudes	1.2
$\mathcal{A}_{\text{intra}}^{(\text{sc})}$		mean self-calibration gain for co-located stations	0.98
$\mathcal{A}_{\text{LMT}}^{(\text{sc})}$		LMT mean self-calibration gain	1.15
$\mathcal{A}_{\text{SMT}}^{(\text{sc})}$		SMT mean self-calibration gain	1.01
$\mathcal{A}_{\text{SPT}}^{(\text{sc})}$		SPT mean self-calibration gain	1.00

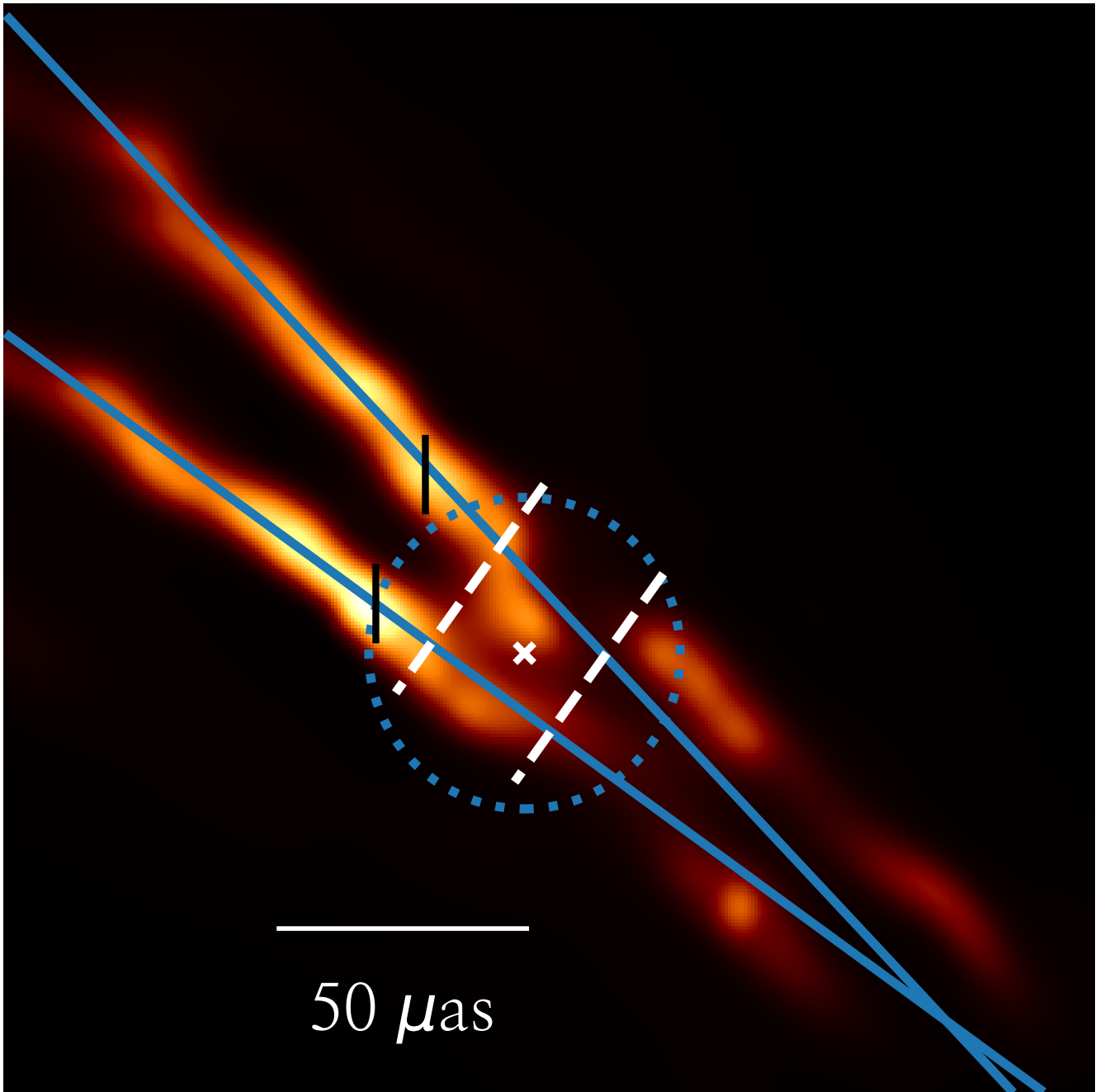
Note – $\mathcal{A}_{\text{intra}}^{(\text{sc})}$ corresponds to the mean gain of ALMA, APEX, JCMT, and SMA.



Supplementary Figure 7: Cen A data properties from April 2017. The top left panel shows the (u, v) coverage. A priori calibrated amplitude (before self-calibration) and closure phase data points are shown in the top right and bottom panel, respectively, overplotted with lines from the final image model as a function of (u, v) distances. The error bars indicate thermal noise and 5% non-closing error uncertainties added in quadrature, which are smaller than the plotted symbols in some cases. The color-coding shows different baselines. Amplitudes projected along and perpendicular to the jet position angle are given in Supplementary Fig. 8.



Supplementary Figure 8: Source structure along specific position angles on the sky. A priori calibrated amplitudes are shown projected along the jet position angle (PA) on the sky in the left panel and perpendicular to the PA in the right panel. The color coding and error bars shown are the same as in Supplementary Fig. 7.



Supplementary Figure 9: Determination of the jet apex location. A zoomed-in version of the final image model is shown. The solid blue lines show simple linear extrapolations of the inner NW and SE jet arms, which would place the jet apex well within the counterjet region. The dashed white lines mark the certain edges of the approaching jet and the counterjet. The quadrangle enclosed by the solid and dashed lines is the region where the jet apex is located. Inside this quadrangle, a tentative convergence of the two streamlines can be seen. The apex position assumed in this work is indicated with a white cross. The surrounding blue dashed circle corresponds to the $z_{\text{col}} = 32 \mu\text{as}$ distance. Vertical black bars mark the brightest regions along each jet arm, which correspond to the assumed location of the radio core.